Sinusoidal voltage protocols for rapid characterization of ion channel kinetics

Kylie A. Beattie Ph.D.[1,2], Adam P. Hill Ph.D.[3,4], Rémi Bardenet Ph.D.[5], Yi Cui Ph.D.[6], Jamie I. Vandenberg Ph.D.[3,4], David J. Gavaghan Ph.D.[1], Teun P. de Boer Ph.D.[7], Gary R. Mirams Ph.D.[8]

September 29, 2017

1. Computational Biology, Department of Computer Science, University of Oxford, OX1 3QD, UK.
2. Division of Applied Regulatory Science, Office of Clinical Pharmacology, Office of Translational Sciences, Center for Drug Evaluation and Research, Food and Drug Administration, Silver Spring, MD, USA.
3. Department of Molecular Cardiology and Biophysics, Victor Chang Cardiac Research Institute, Sydney, NSW 2010, Australia.
4. St Vincent's Clinical School, UNSW Sydney, Darlinghurst, NSW 2010, Australia.
5. CNRS & CRIStAL, Université de Lille, 59651 Villeneuve d'Ascq, France.
6. Safety Evaluation and Risk Management, Global Clinical Safety and Pharmacovigilance, GlaxoSmithKline, Uxbridge, UB11 1BS, UK.
7. Department of Medical Physiology, Division of Heart & Lungs, University Medical Center Utrecht, Utrecht, The Netherlands.
8. Centre for Mathematical Medicine & Biology, School of Mathematical Sciences, University of Nottingham, NG7 2RD, UK.

Short Title: Sinusoidal protocols capture ion channel kinetics

Corresponding Author: Gary Mirams `<gary.mirams@nottingham.ac.uk>`
Mathematical Sciences,
University Park,
Nottingham,
NG7 2RD,
United Kingdom.

Word Count: 6620
Subject Terms: Ion Channels/Membrane Transport; Electrophysiology; Computational Biology.

Abstract

Rationale: Understanding the roles of ion currents is crucial to predict the action of pharmaceuticals and mutations in different scenarios, and thereby to guide clinical interventions in the heart, brain and other electrophysiological systems. Our ability to predict how ion currents contribute to cellular electrophysiology is in turn critically dependent on our characterization of ion channel kinetics — the voltage-dependent rates of transition between open, closed and inactivated channel states.

Objective: The hERG potassium channel plays a fundamental role in controlling electrical activity in the heart and many other tissues. There is a well-established link between hERG mutations, or block by pharmaceuticals, and increased arrhythmic risk. We present a new method for rapidly exploring and characterizing ion channel kinetics, applying it to the hERG channel as an example, with the aim of generating a quantitatively predictive representation of the ion current.

Methods & Results: We fit a mathematical model to currents evoked by a novel 8 second sinusoidal voltage clamp in CHO cells over-expressing hERG1a. The model is then used to predict over 5 minutes of recordings in the same cell in response to further protocols: a series of traditional square step voltage clamps, and also a novel voltage clamp comprised of a collection of physiologically-relevant action potentials. We demonstrate that we can make predictive cell-specific models that outperform the use of averaged data from a number of different cells, and thereby examine which changes in gating are responsible for cell-cell variability in current kinetics.

Conclusions: Our technique allows rapid collection of consistent and high quality data, from single cells, and produces more predictive mathematical ion channel models than traditional approaches. The approach will be widely applicable to other voltage-gated ion currents both in the heart and other electrophysiological systems.

Keywords: hERG, I_{Kr}, mathematical model, electrophysiology, patch clamp, voltage protocol

Non-standard Abbreviations and Acronyms

- CHO — Chinese Hamster Ovary [cells].
- G_{Kr} — maximal conductance of I_{Kr}.
- HEK — Human Embryonic Kidney [cells].
- hERG — human Ether-a-go-go Related Gene.
- I_{Kr} — rapid delayed rectifying potassium current, carried by the $K_v11.1$ ion channel whose primary subunit is encoded by hERG.

1 Introduction

Mathematical models of ion channels are a quantitative expression of our understanding of ion channel kinetics: they express the probability of channels existing in different conformational states (typically, closed, open and inactivated) and the rates of transition between these states[1,2]. Parameterizing/calibrating a mathematical model of an ion current is a concise way to characterize ion channel kinetics, to capture our understanding in a quantitative framework, and to communicate this knowledge to others. There have been some notable advances in deriving mathematical models for ion channel behavior[3–7], with some stressing the need for validation/testing of the model using data from the same cell[8]. In this paper we present a new approach for characterizing ion channel kinetics, using novel short protocols and parameter inference techniques to construct an ion channel model.

The *KCNH2* gene (also known as *hERG*) has been shown to encode the primary subunit of the voltage-gated ion channel Kv11.1 that carries the rapid delayed rectifier potassium current (I_{Kr})[9,10]. In this article we focus on mathematical modeling of hERG channel kinetics, demonstrating our approach by constructing an improved model of this ion current. hERG plays important roles in the brain[11]; gastrointestinal tract[12]; uterine contractions[13]; cell-proliferation and apoptosis[14] and cancer progression[15], but I_{Kr} is best known as a repolarizing cardiac ion current. The channel is susceptible to binding and blockade by pharmaceutical compounds, which is strongly linked to many cases of drug-induced pro-arrhythmic risk[16,17]. Mathematical modeling of cardiac electrophysiology, including I_{Kr}, forms a core part of a new proposal for routine *in vitro* and *in silico* safety assessment to replace a human clinical drug safety study[18,19]. A wide range of different mathematical models have been proposed to describe I_{Kr} (details of literature models are given in Online Supplement A, Table A1). These models were developed to describe different species, cell types, temperatures and isoforms, so variation is expected. Figure 1A shows predicted current under three different voltage clamps for 29 literature models. Unfortunately, even models for the same conditions do not provide consistent predictions.

The first models of ion channel kinetics were proposed by Hodgkin & Huxley[20], and relatively little has changed in the methods used for construction of mathematical models of ion channel gating since the original seminal work in 1952. The traditional approach is to fit peak currents and time constants of current activation/decay after clamping to fixed voltages; to assemble current/voltage (IV) and time-constant/voltage (τ–V) curves; and to describe these curves with interpolating functions.

Condensed voltage clamp step protocols have been suggested as the basis of optimized experiments that provide information about ion channel kinetics faster than experiments to construct IV curves[21,22]; and optimized current and square step voltage clamps have been used to optimize the fitting of maximal conductances in action potential models[23]. Single sinusoid voltage clamps have been previously been explored for choosing between possible Shaker channel models that were parameterized using traditional square step voltage clamps[24].

In this study, we extend these ideas and propose an 8 second sinusoid-based voltage protocol, designed to explore the kinetics of the hERG channel, and use this protocol to record currents from Chinese Hamster Ovary (CHO) cells that are over-expressing hERG1a. These recordings are then used to parameterize a mathematical model of the ion current. We then evaluate the model by predicting the response to both standard square step voltage-clamp protocols and physiologically-relevant action potential voltage clamps: an extremely thorough independent validation for a model of ion channel kinetics. Our approach uses a substantially shorter experimental recording to construct the ion channel model than the usual approach based on time constants and peak currents from a series of square step voltage-clamp protocols. As a consequence of the high information

content of the short protocol, we are able to generate cell-specific models that advance our understanding of variability of ion currents between cells. Our methodology will be applicable to many ion channels, both in the heart and other electrophysiological systems.

2 Methods

2.1 Experimental methods

We performed whole-cell patch-clamp voltage clamp experiments, using CHO cells stably expressing hERG1a (Kv11.1) at room temperature. Full details including cell culture, solutions, and equipment settings can be found in Online Supplement B. In Figure 1B we provide an overview of the experimental approach, denoting the sequence of voltage clamp protocols we performed as Pr0–Pr7.

In each cell we recorded: a series of conventional voltage-step protocols designed to explore activation (Pr1–3), inactivation (Pr4) and deactivation (Pr5); a new protocol composed of a series of action potential clamps (Pr6 — formed of simulated action potentials from different mathematical models to represent diverse species and pacing frequencies in both healthy and repolarization-failure conditions); and our new 8 s sinusoidal voltage protocol (Pr7, shown in Figure 2). These protocols are all performed in a single experiment using a single cell, and the process can be repeated in different cells. A mathematical model is then fitted/calibrated to solely the current provoked by the sinusoidal protocol, and this model then represents a full characterisation of I_{Kr} in each particular cell. The characterisation is then tested for accuracy by using the fitted mathematical model to predict the results of all the other voltage clamp protocols performed in that cell. Full details of all protocols are given in Online Supplement B1.4.

In all protocols, the holding potential was initially −80 mV before applying a 50 ms leak step to −120 mV before returning back to −80 mV, with this step being used to estimate leak current (as described below in Section 2.2). A voltage step to −120 mV at the end of all the protocols ensures that channels close quickly, reducing the time needed between protocols to regain a steady closed state.

Protocols 0 to 5 — Square Step Clamps

Protocol 0 is a simple repeated activation pulse designed to open the channel to visually test the recordings were stable and to allow dofetilide binding, considered open state dependent, to occur (see Section 2.3, below). This current was not recorded or used in the subsequent analysis (hence 'Protocol 0').

Protocols 1–5 are adaptations of 'traditional' square step voltage clamps used in previous studies to examine activation (Pr1–3), inactivation (Pr4) and deactivation (Pr5). Details of the protocol voltages and timings can be found in Online Supplement B1.4.

Note that protocols 1–5 are shorter than some of those which have previously been used to calibrate mathematical models (as in fewer test voltages/timings are used) in order to perform them all in a single cell, with and without dofetilide subtraction, so a 'traditional approach' would take longer than the experiments performed here, generally requiring multiple cells.

Protocol 6 — Action Potentials Clamp

This protocol was formed by combining a series of different simulated action potentials from the Cardiac Electrophysiology Web Lab[25]. The range of models we used for the simulations encompassed different cell types, species, and pacing rates. We also added some simulated action potentials where early or delayed after-depolarizations had been induced, to test I_{Kr} behaviour in pro-arrhythmic or

pathological settings. The action potentials were shifted slightly so that their resting potentials were exactly $-80\,\mathrm{mV}$ (see the Supplementary Code for full details and code to reproduce this protocol).

Protocol 7 — Sinusoidal Clamp

The protocol used to characterise the current and train the model is a voltage clamp comprised of simple steps and a main sinusoidal section that is in the form of a sum of three sine waves of different amplitudes and frequencies, designed to rapidly explore hERG channel kinetics. The underlying rationale is to force the protocol to 'sweep' both the time and voltage dependence of the current gating over physiological voltage ranges.

The start of the protocol takes the form of a leak step followed by a simple activation step which is similar to Protocol 0. This activation step was included to improve the identifiability of the maximal conductance parameter (as described in Online Supplement B2.2) after preliminary experiments suggested this might improve what is known as 'parameter identifiability' (to pin down possible values of the parameter more accurately, and prevent other kinetic parameters compensating for an inaccurate conductance value).

The main sinusoidal portion of the protocol takes the form of a sum of three sine waves as shown in Equation (1):

$$V(t) = -30 + A_1 \sin(\omega_1(t - t_0)) + A_2 \sin(\omega_2(t - t_0)) + A_3 \sin(\omega_3(t - t_0)), \tag{1}$$

where $A_1 = 54\,\mathrm{mV}$, $A_2 = 26\,\mathrm{mV}$, $A_3 = 10\,\mathrm{mV}$, $\omega_1 = 0.007\,\mathrm{ms}^{-1}$, $\omega_2 = 0.037\,\mathrm{ms}^{-1}$ and $\omega_3 = 0.19\,\mathrm{ms}^{-1}$, and t is time measured in milliseconds.

In terms of frequencies, existing models and $\mathrm{I_{Kr}}$ recordings include characteristic timescales of order 10 ms to one second[26,27]. Therefore we designed the sinusoidal protocol's three frequencies to probe channel kinetics across all these orders of magnitude (10 ms, 100 ms and 1 s timescales). We selected frequencies that were co-prime rather than exactly multiples of ten: ω_1 to ω_3 are ordered slow to fast and correspond approximately to sine waves of period 900, 170 and 33 ms, respectively. The aim was that the three distinct frequencies should not become 'in phase': the protocol never repeats patterns that the cell has experienced before (ensuring new information is supplied throughout). The offset t_0 is 2500 ms as explained in Online Supplement B1.4. If one was to study other ion channels, these frequencies may need adjustment to examine relevant timescales.

To decide the amplitudes, the oscillations are centered around $-30\,\mathrm{mV}$ so that a physiological range is explored ($-120 < V < 60\,\mathrm{mV}$). The amplitudes of the sine waves were selected to keep the protocol within this range ($A_1 + A_2 + A_3 = 90\,\mathrm{mV}$) and to ensure that $A_1 > A_2 > A_3$ so that the fastest timescale had the smallest oscillations (to avoid the faster gating processes masking the voltage-dependence of slower ones).

A key step in settling on this particular protocol was its performance in 'synthetic data' studies where we simulated $\mathrm{I_{Kr}}$ with different sets of given parameters, then attempted to recover these parameters blindly — using just the generated current trace with added noise, as illustrated in Online Supplement C2 (we also show this for an $\mathrm{I_{Ks}}$ model with the same protocol in Supplement G).

The sinusoidal protocol is of only eight seconds duration, which enables efficient data collection, with training and validation data collected from the same cell. In Figure 2 we present the novel sinusoidal protocol Pr7, the simulated predicted currents from existing models, and the currents we recorded experimentally. The new protocol provokes an even wider array of different behaviors from the existing literature $\mathrm{I_{Kr}}$ models (middle panels in Figure 2) than the existing voltage step or action potential clamps (Figure 1A); even among models constructed in/for similar conditions/species.

2.2 Leak Corrections

We used the leak-step from $-80\,\mathrm{mV}$ to $-120\,\mathrm{mV}$ in order to leak-correct the experimental data, according to:

$$I_{\mathrm{corrected}} = I_{\mathrm{raw}} - V/R_{\mathrm{leak}}. \tag{2}$$

We identified the most appropriate R_{leak} value to minimize the difference between the mean current value during the leak step (to $-120\,\mathrm{mV}$) compared to the mean value at a holding potential of $-80\,\mathrm{mV}$, whilst ensuring that the trace was not over-corrected (which would result in negative currents during the initial stages of activation).

We manually selected leak resistances to correct the current evoked by the sinusoidal protocol in both vehicle and dofetilide conditions. We then applied this leak resistance to the remaining protocols performed in the same condition on each cell.

The mean current during the $-80\,\mathrm{mV}$ step was calculated from 200 ms of the $-80\,\mathrm{mV}$ holding period before the $-120\,\mathrm{mV}$ leak step (not including the capacitive spike at the point at which the step occurs). The baseline current at a holding potential of $-80\,\mathrm{mV}$ was then adjusted back to 0 nA with a constant additive current if required.

2.3 Dofetilide Subtraction

In preliminary work, we observed that our sinusoidal protocols could elicit endogenous voltage-dependent background currents within expression-system cells. We observed that the levels of endogenous currents the protocols elicited varied from cell to cell. These currents could adversely affect the predictive ability of the resulting mathematical models, as the fitting process attempted to create a model that described both the endogenous and $\mathrm{I_{Kr}}$ components of the recorded currents. To overcome this technical issue we made a number of alterations to our pilot experiments.

Firstly, we constrained the design of the sinusoidal protocol, as discussed above, so that only voltages within a physiological range of $-120\,\mathrm{mV}$ to $+60\,\mathrm{mV}$ were explored, as endogenous currents were much more prominent at voltages above $+60\,\mathrm{mV}$ that we explored in pilot studies.

Secondly, we changed to use CHO cells in this study, rather than the HEK cells we used in pilot studies, as CHO cells generally had lower endogenous currents.

Thirdly, we recorded the full set of voltage protocols (Pr1–7) twice: once in Dimethyl sulfoxide (DMSO) vehicle conditions and once following the addition of $0.3\,\mu\mathrm{M}$ dofetilide, as shown in Figure 1B. Dofetilide was first dissolved in DMSO before being added to the bath solution to produce the required concentration. The required dose of dofetilide was obtained by serial dilution. We chose to use $0.3\,\mu\mathrm{M}$ because the dofetilide hERG $\mathrm{IC_{50}}$ value is $<10\,\mathrm{nM}$ which, assuming a Hill coefficient of one, should correspond to $>97\%$ conductance block of $\mathrm{I_{Kr}}$ at $0.3\,\mu\mathrm{M}$ dofetilide. We avoided higher concentrations as dofetilide does have other known voltage-dependent ion channel targets whose $\mathrm{IC_{50}}$s are in the 10s–100s of μM range[28]. Between the two recordings we allowed the dofetilide-induced current block to reach equilibrium (under Pr0). We then subtracted the currents that remained in the presence of dofetilide from those recorded in the presence of vehicle to remove any contribution of endogenous currents (and to produce what we refer to as 'dofetilide subtracted' data). Prior to performing this subtraction, we first leak subtracted both the vehicle and dofetilide recordings individually, as described above. It may not always be necessary for dofetilide subtraction to be performed on CHO cells, as endogenous voltage-dependent currents can be very low, and leak subtraction may suffice (see Online Supplement B1.6). But we applied the dofetilide subtraction method nonetheless to generate a gold-standard dataset for this study.

2.4 Mathematical Model

Whilst our model is equivalent to a two gate Hodgkin-Huxley formulation[20], we use a Markov model description in practice (simply to generalize the computational code for other model structures). The system of ordinary differential equations underlying the mathematical model structure shown in Figure 3B is then:

$$\frac{\mathrm{d}C}{\mathrm{d}t} = -(k_1 + k_3)C + k_2 O + k_4[IC], \tag{3}$$

$$\frac{\mathrm{d}O}{\mathrm{d}t} = -(k_2 + k_3)O + k_1 C + k_4 I, \tag{4}$$

$$\frac{\mathrm{d}IO}{\mathrm{d}t} = -(k_2 + k_4)I + k_3 O + k_1[IC], \tag{5}$$

where

$$[IC] = 1 - (C + O + I)\,. \tag{6}$$

The eight parameters P_1 to P_8 determine the rates k_1 to k_4 according to the exponential relationships shown in Figure 3B. The current, I_{Kr}, is modeled with a standard Ohmic expression:

$$I_{\mathrm{Kr}} = G_{\mathrm{Kr}} O\,(V - E_K)\,, \tag{7}$$

where G_{Kr} is the maximal conductance, E_K is the Nernst potential for potassium ions, and O is the open probability, given by the solution to the system of equations above. E_K is not inferred, but is calculated directly from the ratio of ion concentrations on each side of the cell membrane using the Nernst equation:

$$E_K = \frac{RT}{zF} \ln\left(\frac{[K]_{\mathrm{out}}}{[K]_{\mathrm{in}}}\right). \tag{8}$$

where R is the ideal gas constant, T is the temperature, F is the Faraday constant, z is the valency of the ions (in this case 1), and $[K]$ represents the concentration of potassium ions. Note that this expression has a temperature dependence, and the temperature of the bath was recorded for each cell and used in relevant simulations.

All simulations were performed in MatLab. Mex functions were used to define the equations and simulate by using CVODE[29] to solve the systems of differential equations, with both absolute and relative tolerances set to 10^{-8}. Code is available to download as described at the end of the manuscript.

2.5 Parameter Inference

We used a global minimization algorithm[33] followed by a custom-written Bayesian inference method. Following Siekmann *et al.*[6], parameters were estimated using a Monte Carlo based inference scheme, in this case using an approach similar to that described in Johnstone *et al.*[30]. In Online Supplement B2 we give details of how: (1) a likelihood is assigned to any candidate parameter set; (2) maximizing the likelihood using a global optimization scheme gives a 'best fit' parameter set; (3) uniform prior distributions are assigned to the kinetic parameters; and (4) we start a Markov chain Bayesian inference scheme from the estimated global optimum to generate a posterior probability distribution. The benefits of this scheme are that we explore the 'parameter space' widelyand build up a probability distribution (probability of parameters generating the experimental results we observed) across the whole parameter space. This posterior distribution allows us to check that we are constraining each parameter's value with the information in the experiment, and are not experiencing problems with identifiability of parameters[6].

2.6 Note on Normalization

Where existing literature model simulations were plotted alongside experimental traces, or one experimental trace was compared with another, we first had to normalize to account for differences in conductance values. This was achieved by selecting a scaling factor for the conductance value for each model simulation (or experimental trace) that minimized the square difference between each trace and a reference experimental trace.

For literature models the reference trace was the experimental current from the action potential clamp Pr6. Note this provides a best-case fit to Pr6 for all of the literature models, removing the possibility that some models open 'half as much' because they have 'twice the conductance'. For the new model, no scaling was applied and conductance was directly fitted to the experimental current from the sinusoidal protocol (along with other parameters).

3 Results

3.1 Model Calibration

We calibrate a mathematical model using only data recorded under the sinusoidal protocol (Pr7). The Hodgkin-Huxley[20]-style structure of the model we use, and its corresponding model parameters, can be seen in Figure 3B. We independently fitted this model to each of the experimental current traces shown in Figure 2. For each cell, we obtain a probability distribution of estimates for each parameter that captures any observational uncertainty in the parameter values[31,32].

The result of the fitting procedure for one cell is shown in Figure 3. The parameter set with maximum posterior density is shown in Figure 3A, demonstrating an excellent fit between experimental and simulated data. The resulting posterior probability density for the parameters obtained from this Bayesian inference approach is projected across each parameter in Figure 3C. We also tested that our approach is theoretically appropriate for inferring all parameters by using synthetic data studies, as described in Online Supplement C. The plausible parameter space is very narrow: if multiple parameter set samples are taken from the distribution shown in Figure 3C, the resulting simulated current traces are indistinguishable to the eye. To quantify this, taking 1000 samples we find that the 95% credible intervals for the simulated currents were always within at most either 3.47% or, in absolute terms, 0.0043 nA of the simulated current given by the maximum posterior density parameter set.

The results we present in Figure 3 are from a single cell with a good quality recording and a high signal:noise ratio (this choice of cell, and other cells' predictions, are discussed later). We fit models on a cell-specific basis, and then also use averaged experimental data to create a single 'averaged' model as described in Online Supplement F. We will compare these approaches below. We provide all parameter values with the maximum posterior density for all models in Supplementary Table F11.

3.2 Validation predictions

Having trained our model to eight seconds of experimental data from the sinusoidal protocol Pr7, we now test its ability to predict more than 5 minutes of independent experimental behavior. We predict the current in response to traditional voltage-step protocols Pr1–5 (adapted from those previously used in the literature[1]), and also to a novel physiologically-inspired voltage clamp protocol comprised of multiple action potentials (Pr6). All recordings shown in Figures 3–5 are from the same cell, using the experimental procedure shown in Figure 1B.

To make the predictions for Protocols Pr1–6 we performed simulations using the parameter set with the maximum posterior density in the fit to the sinusoidal protocol (Pr7). As with the

calibration protocol, all the predictions we will discuss below are indistinguishable by eye from the result of taking multiple samples from the distributions in Figure 3C and plotting a prediction for each of these parameter sets. We also compare the predictions from our new model with those from a sample of widely-used literature models[26,34–37].

In Figure 4, we show traditional voltage step protocols, experimental recordings and the simulated predictions from the model. We also show some of the most commonly plotted summary curves for experimental data under these protocols, together with predicted summary curves from both our model and a range of existing literature models (methods used to derive summary plots are given in Methods B1.7, results for Pr1&2 in Online Supplement E). We can predict a wide range of current behavior in response to the standard voltage-step protocols, without having used any of this information to fit the model.

There are a number of points to draw attention to in Figure 4. Firstly, most of the current-voltage relationships and time constant-voltage relationships we predict in response to the traditional voltage-step protocols are closer to the experimental data than similar model-experiment comparisons in the literature (even when existing literature models, with more parameters, were fitted to such data). Secondly, there are some weaknesses to the new model — particularly in predictions of the Pr4 summary plot of time constant (τ) of inactivation against voltage, where we predict a time constant that is approximately 4 ms too fast at -40 mV. Yet, it is worth noting that this may be the best fit that is possible with a Hodgkin-Huxley style model: the Ten Tusscher and Zeng models predict timecourses that are so different it is difficult to fit comparable time constants. The current timecourse for Pr4 is actually predicted more accurately than any of the other models shown here (see Supplementary Table D6) despite the τ-V relationship being less accurate; in agreement with this, other summary IV curves of Pr4 are predicted more accurately by the new model (see Supplementary Figures E9 & E10).

Figure 5 shows the model prediction of the currents invoked in response to the physiologically-inspired action potential protocol Pr6, compared with the experimental recording (as shown in Figure 1B we used the first repeat of Pr6 for validation purposes, and the second as a quality control measure). Replicating behavior under action potentials is perhaps the most important requirement for a hERG channel model for use in physiological or pharmacological studies. The model is able to predict the response to all of the complex action potential protocol extremely well, and much better than existing models (even though we have scaled literature models' maximal conductances (G_{Kr}) to fit this trace as well as possible in Figure 5).

We provide a quantitative comparison of predicted current traces for our model and each of the literature models for Pr3–7 in Supplementary Tables D6. In each case, the worst-performing literature model is a Hodgkin-Huxley style model. Yet our simple model, with the same structure, is able to provide significantly better predictions than even the Markov-type models, which are usually considered to be better representations of hERG kinetics[1]. Our methodology has resulted in a simple and highly predictive mathematical model, able to describe a wide range of physiologically-relevant behavior.

3.2.1 Cell-specific validation

In Figure 6A we present the maximum posterior density parameter values when repeating the above approach using data from nine different cells. The clustered parameter values demonstrate that parameters derived from different cells take similar values, giving us confidence that the procedure is reproducible and biophysically meaningful. There is more cell-to-cell variability in some parameters than others, which may be related to variability in the underlying physiological processes that they represent; supporting the value, and perhaps necessity, of a cell-specific approach. We also

acknowledge that some parameters may be more or less sensitive to variability in experimental conditions such as temperature, residual background/endogenous currents, and imperfect dofetilide and/or leak subtraction.

We order the cells in Figure 6 based on the lowest difference in leak resistance between the vehicle and dofetilide recordings of Pr7. This ordering gives a measure of recording stability, and is intended to be a surrogate for data quality. The cell presented above, in Figures 3–5, corresponds to Cell #5 of 9 under this ranking, so we obtain very good predictions even with our 'median' quality data. We show cell-specific predictions of the current-voltage relationship for the peak steady-state activation current for each cell-specific model in Figure 6B. While we focused on Cell #5 in the results section, Cells #1–4 also produce excellent cell-specific predictions (similar comparisons for other summary plots are in Supplementary Figures F12–F14).

We also investigated the benefit of a cell-specific approach by building a model using averaged experimental data from all nine cells. We describe this approach in Online Supplement F, and summarize the results in Supplementary Table F12. Generally, for the cells with the highest data quality (Cells #1–5) the cell-specific models provide better predictions than the average model, as we see for Pr3 when comparing colored cell-specific predictions and experiment with the black line for the average model in Figure 6B. The same trend holds for the action potential protocol Pr6, in 8/9 cells the cell-specific model provides less error than the average cell model — the largest improvement was 50% less error; for the remaining cell where the average cell model provided better predictions, this was by 3%.

4 Discussion

In this paper we have presented a novel method for constructing mathematical models of ion channel kinetics. We used a sinusoidal voltage protocol to construct a simple model of hERG channel kinetics using just 8 seconds of recording, as opposed to a traditional approach that requires several minutes of voltage-step data. All of our experimental data can be collected from a single cell, whereas a typical approach necessitates the collection of data from a number of different cells. In future, such an approach opens up the possibility of making multiple interventions (such as the addition of drug compounds) since we have shown we could re-measure the full ion channel kinetics multiple times in a single cell.

The conceptual shift is that channel kinetics should be summarized by mathematical model parameters, not a series of current-voltage (IV) and time constant-voltage curves. In essence, the model *is* the current characterization, rather than something designed to fit IV and time constant curves, which only represent a certain subset of possible behaviors of the current.

We saw that our model is able to replicate the experimental training data very well (Figure 3). This is often the point at which literature approaches stop, and conclude that a mathematical model is a good representation of ion channel kinetics (something that is also true more generally for mathematical models of biological processes). Instead, we performed an extremely thorough evaluation of the model by testing its ability to predict the behavior in response to a series of voltage clamp protocols it has not 'seen before' (both those traditionally used to characterize hERG channel kinetics, and also a new complicated series of action potential waveforms), all recorded from the same cell as the training data. We are not aware of such a thorough, physiologically-relevant validation of an ion channel model having been performed before. Testing that we are able to predict the current response to a voltage pattern which may be observed in physiological or patho-physiological conditions is a particularly robust and useful way to validate a model, and critical if an I_{Kr} model is to be used to accurately predict cardiac electrical activity in healthy and

potentially arrhythmic situations.

The extremely good prediction from all our cell-specific models of the response to the complex action potential protocol is particularly remarkable (Figure 5). Cell-to-cell variability in ion channel kinetics was captured by fitting different underlying kinetic parameters. These parameter sets were shown to have modest variation, and this variation in kinetics was quantitatively predictive of variation observed in independent validation experiments (Figure 6). Cell-specific predictions were particularly strong when using the highest quality data, highlighting the necessary data quality for constructing accurate and robust models of ion channel kinetics. The cell-specific models outperformed a model constructed using averaged data from multiple cells/experiments, in line with the 'failure of averaging' discussed in Golowasch *et al.*[38] and the problems of fitting to averaged summary curves outlined in Pathmanathan *et al.*[39].

There are still some aspects of the experimental behavior that are not replicated by our model. In particular, there is only one time constant of deactivation, and low voltage-dependence in the inactivation time constant (Figure 4). But then neither is the full range of behavior captured by any of the existing, more complex, models available in the literature. We have shown that our model can provide better predictions than the literature models for all the raw current timecourses, if not all summary curves, in the majority of cases.

Our inactivation protocol (Pr4) showed that it is possible for models to fit some (or all) summary curves well, without necessarily replicating the underlying current traces with less error. Often studies present just one summary curve in isolation. But we have seen how some models can fit certain summary curves well, whilst fitting other summary curves badly. Models that have less accurate summary curves may predict the underlying current traces more reliably; and, importantly, vice-versa. A focus on these summary curves to represent kinetics and fit mathematical model behavior was necessary in the era of hand fitting parameters using graph paper, but should perhaps now be superseded by fitting/comparing directly to experimental current traces. By fitting directly, we can also reduce the possible influence of subjective choices during the time-constant fitting process used in the generation of time-constant voltage relationships.

The inability of our model to replicate all of the experimental data may be a consequence of using a simple Hodgkin-Huxley model formulation, although it is a commonly used structure for currents within action potential models. A more complicated Markov model may be needed to capture certain behaviors.

However, the simplicity of our model may also be the key to its success — with only eight kinetic parameters we have confidence that they are all being fitted well, and we have shown that there is low uncertainty in their values. As Pathmanathan & Gray[31] and Mirams *et al.*[32] have recently discussed, considering probabilistic uncertainty in our model parameters and predictions is evermore important as models begin to be used for safety-critical predictions such as the Comprehensive in-vitro Proarrhythmia Assay initiative being pursued by the FDA in collaboration with industry, academia and other regulators[18,19], and also clinical applications[40].

A limitation of the model produced by our study is that it was trained on experiments performed in expression line cells, creating a hERG1a model at room temperature; compared to native I_{Kr} current in cardiac cells which will have additional isoforms, subunits and regulation at physiological temperatures. As a result, we cannot confidently state that this ion current model would give better performance in an action potential model. To characterize native I_{Kr} kinetics we plan to apply the methodology presented here in myocytes, to make a model that is more applicable for use in cardiac safety testing and whole-organ simulations.

The success of our approach in different ion channels will be heavily dependent on the precise form of the sinusoidal protocol that is used, and in parallel work we are developing different strategies for optimizing the voltage protocol design for given currents. But we have shown that

the existing sinusoidal protocol is also theoretically appropriate for parameterising an I_{Ks} model in Supplement G. Previously, Bett *et al.*[1] explored the behaviors of a subset of existing hERG channel models and concluded that the model proposed by Wang *et al.*[26] was best able to replicate the activation kinetics of the hERG channel. In other parallel work, we are extending the approach presented here for selecting between different possible model structures for hERG channel kinetics (see Online Supplement Figure A1 for the range of possibilities).

In summary, we have demonstrated significant advantages in our cell-specific mathematical modeling approach, observing excellent model predictions of currents in response to protocols the model was not trained to replicate. Therefore, the simple ion channel state arrangement we have assumed captures the most important features underlying ion channel state transitions well, despite being much simpler than many previous models in the literature. The information-rich approach allows, for perhaps the first time, an exploration of both within-cell and between-cell variability in ion channel kinetics. The significant time saving of our short protocol leads to datasets that are more consistent and therefore of higher quality, since little changes in experimental conditions during the 8 second recording interval. Its brevity opens up the possibility of taking more recordings in different experimental conditions within a single cell (e.g. drug concentrations[41,42] or temperatures[43]). These datasets will result in more accurate descriptions of ionic currents in these different conditions in the heart and other organ systems.

Acknowledgments

Our thanks to Prof. Gail Robertson of University of Wisconsin–Madison for assistance in acquiring the cell line used in pilot stages of this study. We would also like to thank the following people for technical assistance, access to facilities, support and encouragement: Jim Louttit, Nick McMahon, Carol Wilson, Sam Turner, Kate Harris and Sara Graham of GSK Safety Assessment; Jules Hancox of University of Bristol; Monique Windley and Mark Hunter of Victor Chang Cardiac Research Institute; Rianne Rijken and Birgit Goversen of UMC Utrecht. Thanks to Ross Johnstone (University of Oxford) for removing singularities from the Zeng model, and to Frank Ball (University of Nottingham) for comments on a paper draft.

Sources of Funding

KAB was supported by the EPSRC and GlaxoSmithKline Plc (grant numbers EP/G037280/1, EP/I017909/1 and EP/K503769/1). JIV and APH acknowledge funding from the NHMRC. RB acknowledges support from ANR grant BoB ANR-16-CE23-0003. GRM gratefully acknowledges support from a Sir Henry Dale Fellowship jointly funded by the Wellcome Trust and the Royal Society (grant number 101222/Z/13/Z).

Author Contributions

KAB, RB, YC, DJG, TdeB, GRM designed the study and modeling approach; KAB, RB & GRM designed and implemented the statistical methods; KAB, GRM, JIV, APH and TdeB designed and refined the experimental methods; KAB performed all the experiments, simulations and statistical analysis; KAB, TdeB, GRM wrote the manuscript; all authors approved the final version of the manuscript.

Disclosures

The authors declare that the research was conducted in the absence of any commercial or financial relationships that could be construed as a potential conflict of interest. The opinions presented here are those of the authors. No official support or endorsement by the Food & Drug Administration is intended nor should be inferred.

Materials & Correspondence

All computational codes, and the experimental current recordings that were used for calibration and validation (leak and dofetilide subtracted), are openly available in a Supplementary Data repository at `https://github.com/mirams/sine-wave`. A permanently archived version is available on Figshare at `https://doi.org/10.6084/m9.figshare.4704550.v3` alongside the full raw data (in both plain text and pClamp formats) at `https://doi.org/10.6084/m9.figshare.4702546.v1`.

References

1. Bett, G. C., Zhou, Q. & Rasmusson, R. L. Models of HERG Gating. *Biophysical Journal* **101,** 631–642 (2011).
2. Vandenberg, J., Perry, M., Perrin, M., Mann, S., Ke, Y. & Hill, A. hERG K+ channels: Structure, function, and clinical significance. *Physiological Reviews* **92,** 1393–1478 (2012).
3. Balser, J. R., Roden, D. M. & Bennett, P. B. Global parameter optimization for cardiac potassium channel gating models. *Biophysical Journal* **57,** 433–44 (Mar. 1990).
4. Cannon, R. C. & D'Alessandro, G. The ion channel inverse problem: neuroinformatics meets biophysics. *PLoS Comput Biol* **2,** e91 (2006).
5. Siekmann, I., Wagner, L. E., Yule, D., Fox, C., Bryant, D., Crampin, E. J. & Sneyd, J. MCMC estimation of Markov models for ion channels. *Biophysical Journal* **100,** 1919–29 (Apr. 2011).
6. Siekmann, I., Sneyd, J. & Crampin, E. J. MCMC can detect nonidentifiable models. *Biophysical Journal* **103,** 2275–86 (Dec. 2012).
7. Loewe, A., Wilhelms, M., Schmid, J., Krause, M. J., Fischer, F., Thomas, D., Scholz, E. P., Dössel, O. & Seemann, G. Parameter Estimation of Ion Current Formulations Requires Hybrid Optimization Approach to Be Both Accurate and Reliable. *Frontiers in Bioengineering and Biotechnology* **3,** 209 (Jan. 2015).
8. Tomaiuolo, M., Bertram, R., Leng, G. & Tabak, J. Models of Electrical Activity: Calibration and Prediction Testing on the Same Cell. *Biophysical Journal* **103,** 2021–2032 (2012).
9. Trudeau, M. C., Warmke, J. W., Ganetzky, B. & Robertson, G. A. HERG, a human inward rectifier in the voltage-gated potassium channel family. *Science* **269,** 92 (1995).
10. Sanguinetti, M., Jiang, C., Curran, M. & Keating, M. A mechanistic link between an inherited and an acquired cardiac arrthytmia: HERG encodes the IKr potassium channel. *Cell* **81,** 299–307 (1995).
11. Babcock, J. J. & Li, M. hERG channel function: beyond long QT. *Acta Pharmacologica Sinica* **34,** 329–35 (2013).
12. Farrelly, A. M., Ro, S., Callaghan, B. P., Khoyi, M. A., Fleming, N., Horowitz, B., Sanders, K. M. & Keef, K. D. Expression and function of KCNH2 (HERG) in the human jejunum. *American Journal of Physiology. Gastrointestinal and Liver Physiology* **284,** G883–95 (2003).

13. Parkington, H. C., Stevenson, J., Tonta, M. A., Paul, J., Butler, T., Maiti, K., Chan, E.-C., Sheehan, P. M., Brennecke, S. P., Coleman, H. A. & Smith, R. Diminished hERG K+ channel activity facilitates strong human labour contractions but is dysregulated in obese women. *Nature communications* **5,** 4108 (2014).

14. Jehle, J., Schweizer, P. A., Katus, H. A. & Thomas, D. Novel roles for hERG K(+) channels in cell proliferation and apoptosis. *Cell Death & Disease* **2,** e193 (2011).

15. Lastraioli, E., Perrone, G., Sette, A., Fiore, A., Crociani, O., Manoli, S., D'Amico, M., Masselli, M., Iorio, J., Callea, M., Borzomati, D., Nappo, G., Bartolozzi, F., Santini, D., Bencini, L., Farsi, M., Boni, L., Di Costanzo, F., Schwab, A., Onetti Muda, A., Coppola, R. & Arcangeli, A. hERG1 channels drive tumour malignancy and may serve as prognostic factor in pancreatic ductal adenocarcinoma. *British Journal of Cancer* **112,** 1076–87 (2015).

16. Redfern, W., Carlsson, L., Davis, A., Lynch, W., MacKenzie, I., Palethorpe, S., Siegl, P., Strang, I., Sullivan, A., Wallis, R., *et al.* Relationships between preclinical cardiac electrophysiology, clinical QT interval prolongation and torsade de pointes for a broad range of drugs: Evidence for a provisional safety margin in drug development. *Cardiovascular Research* **58,** 32 (2003).

17. Pollard, C. E., Abi-Gerges, N., Bridgland-Taylor, M. H., Easter, A., Hammond, T. G. & Valentin, J. P. An introduction to QT interval prolongation and non-clinical approaches to assessing and reducing risk. *British Journal of Pharmacology* **159,** 12–21 (2010).

18. Sager, P., Gintant, G., Turner, J., Pettit, S. & Stockbridge, N. Rechanneling the cardiac proarrhythmia safety paradigm: a meeting report from the Cardiac Safety Research Consortium. *American Heart Journal* **167,** 292–300 (2014).

19. Fermini, B., Hancox, J. C., Abi-Gerges, N., Bridgland-Taylor, M., Chaudhary, K. W., Colatsky, T., Correll, K., Crumb, W., Damiano, B., Erdemli, G., Gintant, G., Imredy, J., Koerner, J., Kramer, J., Levesque, P., Li, Z., Lindqvist, A., Obejero-Paz, C. A., Rampe, D., Sawada, K., Strauss, D. G. & Vandenberg, J. I. A New Perspective in the Field of Cardiac Safety Testing through the Comprehensive In Vitro Proarrhythmia Assay Paradigm. *Journal of Biomolecular Screening* **21,** 1–11 (2016).

20. Hodgkin, A. L. & Huxley, A. F. A quantitative description of membrane current and its application to conduction and excitation in nerve. *Journal of Physiology* **117,** 500–544 (1952).

21. Hobbs, K. H. & Hooper, S. L. Using complicated, wide dynamic range driving to develop models of single neurons in single recording sessions. *Journal of Neurophysiology* **99,** 1871–1883 (2008).

22. Fink, M. & Noble, D. Markov models for ion channels: versatility versus identifiability and speed. *Philosophical Transactions of the Royal Society A* **367,** 2161–2179 (2009).

23. Groenendaal, W., Ortega, F. A., Kherlopian, A. R., Zygmunt, A. C., Krogh-Madsen, T. & Christini, D. J. Cell-Specific Cardiac Electrophysiology Models. *PLoS Computational Biology* **11,** e1004242 (Apr. 2015).

24. Kargol, A., Hosein-Sooklal, A., Constantin, L. & Przestalski, M. Application of oscillating potentials to the Shaker potassium channel. *General Physiology and Biophysics* **23,** 53–76 (2004).

25. Cooper, J., Scharm, M. & Mirams, G. R. The cardiac electrophysiology web lab. *Biophysical Journal* **110,** 292–300 (2016).

26. Wang, S., Liu, S., Morales, M., Strauss, H. & Rasmusson, R. A quantitative analysis of the activation and inactivation kinetics of HERG expressed in Xenopus oocytes. *Journal of Physiology* **502,** 45–60 (1997).

27. Zhou, Z., Gong, Q., Ye, B., Fan, Z., Makielski, J. C., Robertson, G. A. & January, C. T. Properties of HERG channels stably expressed in HEK 293 cells studied at physiological temperature. *Biophysical Journal* **74,** 230–241 (1998).

28. Mirams, G. R., Cui, Y., Sher, A., Fink, M., Cooper, J., Heath, B., McMahon, N., Gavaghan, D. & Noble, D. Simulation of multiple ion channel block provides improved early prediction of compounds' clinical torsadogenic risk. *Cardiovascular Research* **91,** 53 (2011).

29. Hindmarsh, A., Brown, P., Grant, K., Lee, S., Serban, R., Shumaker, D. & Woodward, C. SUNDIALS: Suite of nonlinear and differential/algebraic equation solvers. *ACM Trans. Math. Software (TOMS)* **31,** 363–396 (2005).

33. Hansen, N., Muller, S. & Koumoutsakos, P. Reducing the time complexity of the derandomized evolution strategy with covariance matrix adaptation (CMA-ES). *Evolutionary Computation* **11,** 1–18 (2003).

30. Johnstone, R. H., Chang, E. T., Bardenet, R., de Boer, T. P., Gavaghan, D. J., Pathmanathan, P., Clayton, R. H. & Mirams, G. R. Uncertainty and variability in models of the cardiac action potential: Can we build trustworthy models? *Journal of Molecular and Cellular Cardiology* **96,** 49–62 (2016).

31. Pathmanathan, P. & Gray, R. A. Ensuring reliability of safety-critical clinical applications of computational cardiac models. *Frontiers in Physiology* **4,** 1–9 (2013).

32. Mirams, G. R., Pathmanathan, P., Gray, R. A., Challenor, P. & Clayton, R. H. White paper: Uncertainty and variability in computational and mathematical models of cardiac physiology. *The Journal of Physiology* **594,** 6833–6847 (2016).

34. Zeng, J., Laurita, K. R., Rosenbaum, D. S. & Rudy, Y. Two components of the delayed rectifier K+ current in ventricular myocytes of the guinea pig type theoretical formulation and their role in repolarization. *Circulation Research* **77,** 140–152 (1995).

35. Mazhari, R., Greenstein, J., Winslow, R., Marbán, E. & Nuss, H. Molecular interactions between two Long-QT syndrome gene products, HERG and KCNE2, rationalized by in vitro and in silico analysis. *Circulation Research* **89,** 33–38 (2001).

36. Ten Tusscher, K., Noble, D., Noble, P. & Panfilov, A. A model for human ventricular tissue. *American Journal of Physiology-Heart and Circulatory Physiology* **286,** H1573–H1589 (2004).

37. Di Veroli, G., Davies, M., Zhang, H., Abi-Gerges, N. & Boyett, M. High-throughput screening of drug-binding dynamics to HERG improves early drug safety assessment. *American Journal of Physiology-Heart and Circulatory Physiology* **304,** H104–H117 (2013).

38. Golowasch, J., Goldman, M. S., Abbott, L. & Marder, E. Failure of averaging in the construction of a conductance-based neuron model. *Journal of Neurophysiology* **87,** 1129–1131 (2002).

39. Pathmanathan, P., Shotwell, M. S., Gavaghan, D. J., Cordeiro, J. M. & Gray, R. A. Uncertainty quantification of fast sodium current steady-state inactivation for multi-scale models of cardiac electrophysiology. *Progress in biophysics and molecular biology* **117,** 4–18 (2015).

40. Arevalo, H. J., Vadakkumpadan, F., Guallar, E., Jebb, A., Malamas, P., Wu, K. C. & Trayanova, N. A. Arrhythmia risk stratification of patients after myocardial infarction using personalized heart models. *Nature Communications* **7,** 11437 (2016).

41. Pearlstein, R. A., MacCannell, K. A., Erdemli, G., Yeola, S., Helmlinger, G., Hu, Q.-Y., Farid, R., Egan, W., Whitebread, S., Springer, C., Beck, J., Wang, H.-R., Maciejewski, M., Urban, L. & Duca, J. S. Implications of Dynamic Occupancy, Binding Kinetics, and Channel Gating Kinetics for hERG Blocker Safety Assessment and Mitigation. *Current Topics in Medicinal Chemistry* **16,** 1792–818 (2016).

42. Lee, W., Mann, S. A., Windley, M. J., Imtiaz, M. S., Vandenberg, J. I. & Hill, A. P. In silico assessment of kinetics and state dependent binding properties of drugs causing acquired LQTS. *Progress in Biophysics and Molecular Biology* **120,** 89–99 (2016).

43. Vandenberg, J. I., Varghese, A., Lu, Y., Bursill, J. A., Mahaut-Smith, M. P. & Huang, C. L.-H. Temperature dependence of human ether-a-go-go-related gene K+ currents. *American Journal of Physiology: Cell physiology* **291,** C165–75 (2006).

Figures

A

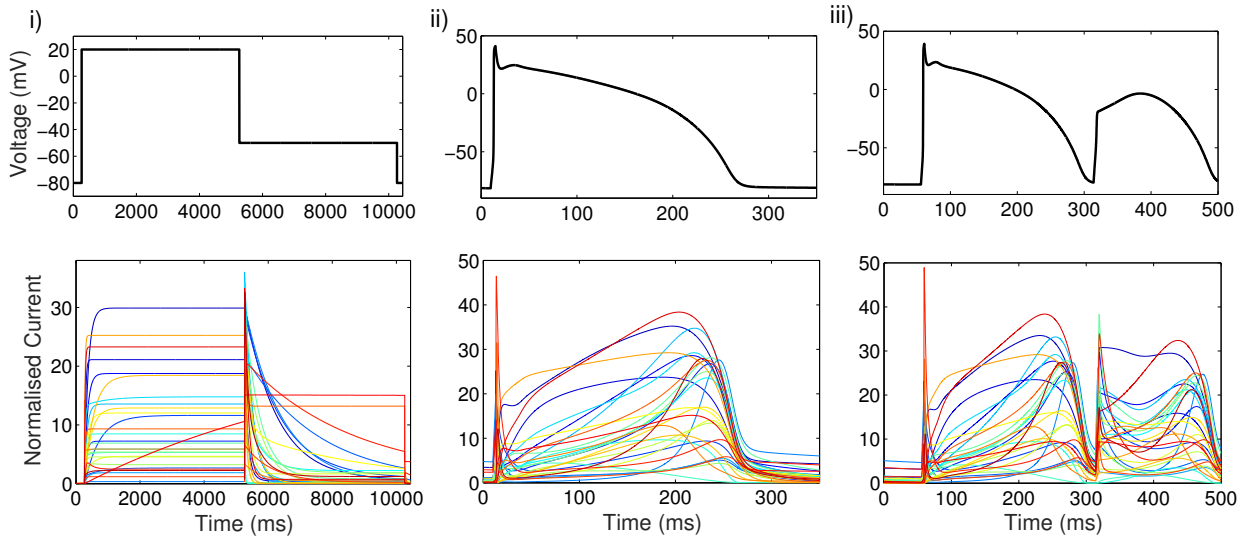

B

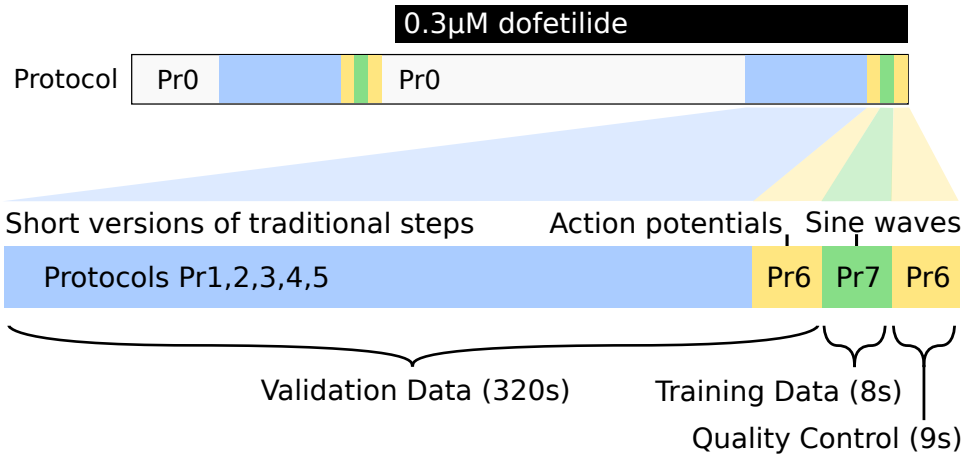

Figure 1: **Current predictions from literature models of I_{Kr}, and diagram of the experimental procedure used in this study**. **A:** predictions from 29 literature models of I_{Kr} in response to different voltage-clamp protocols: (i) a voltage-step; (ii) an action potential; and (iii) an action potential displaying pathological properties. Currents are normalized such that the maximal conductance is equal to one; i.e. we plot the open probability multiplied by the driving voltage (model references are listed in Table A1 in Online Supplement A). All models have been simulated with their original published parameters, with a temperature of 21.5°C and our experimental concentrations used for calculating the reversal potential. **B:** top — a schematic representation of the experimental procedure used for this study over time (not to scale). A simple activation step protocol is repeated in the sections marked 'Pr0', before moving on to the highlighted section (enlarged below) where data used in the study were recorded. The recording protocols 'Pr1–7' are performed twice, once before dofetilide addition, and once after, with the hERG current isolated by subtraction. For full details of the protocols please refer to Methods B1.4.

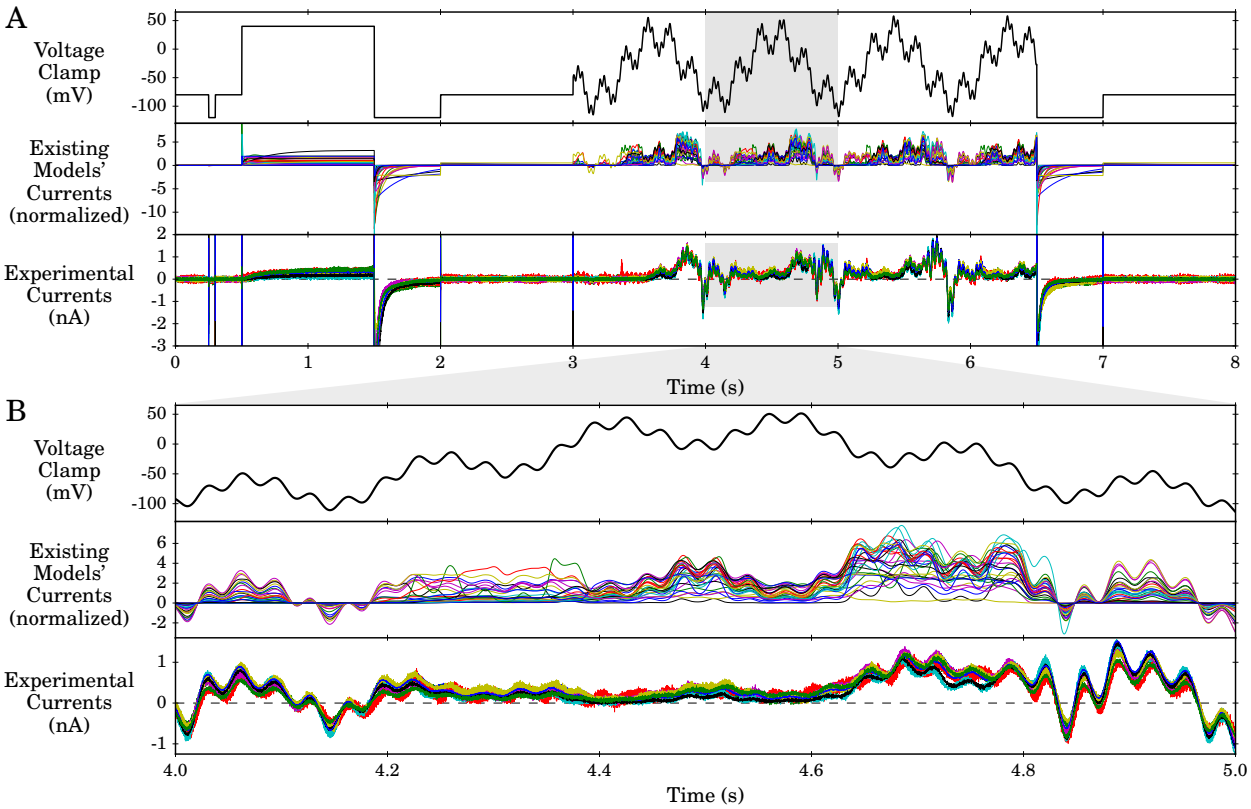

Figure 2: **The sinusoidal protocol and example recordings. A: Top row**: The full sinusoidal voltage protocol (Pr7). **Middle row**: Simulations of expected behavior in response to this protocol from existing I_{Kr} and hERG models, normalized by scaling the conductance value for each model to minimize the absolute difference between each trace and a reference trace. For calculation of the reversal potential, a temperature of 21.5 °C was used to match the mean experimental conditions. **Bottom row**: Raw data (following leak and dofetilide subtraction) from experimental repeats at room temperature from 9 cells. Experimental traces have been scaled, to remove the effect of different maximal conductances, by a factor chosen to minimize the absolute differences between each trace and a reference experimental trace (that with the peak current during the sinusoidal portion of Pr7). **B:** an enlargement of the highlighted sections of panel A. Whilst there is some variation between cells in the experimental results, they are much more consistent than the predictions from the different models.

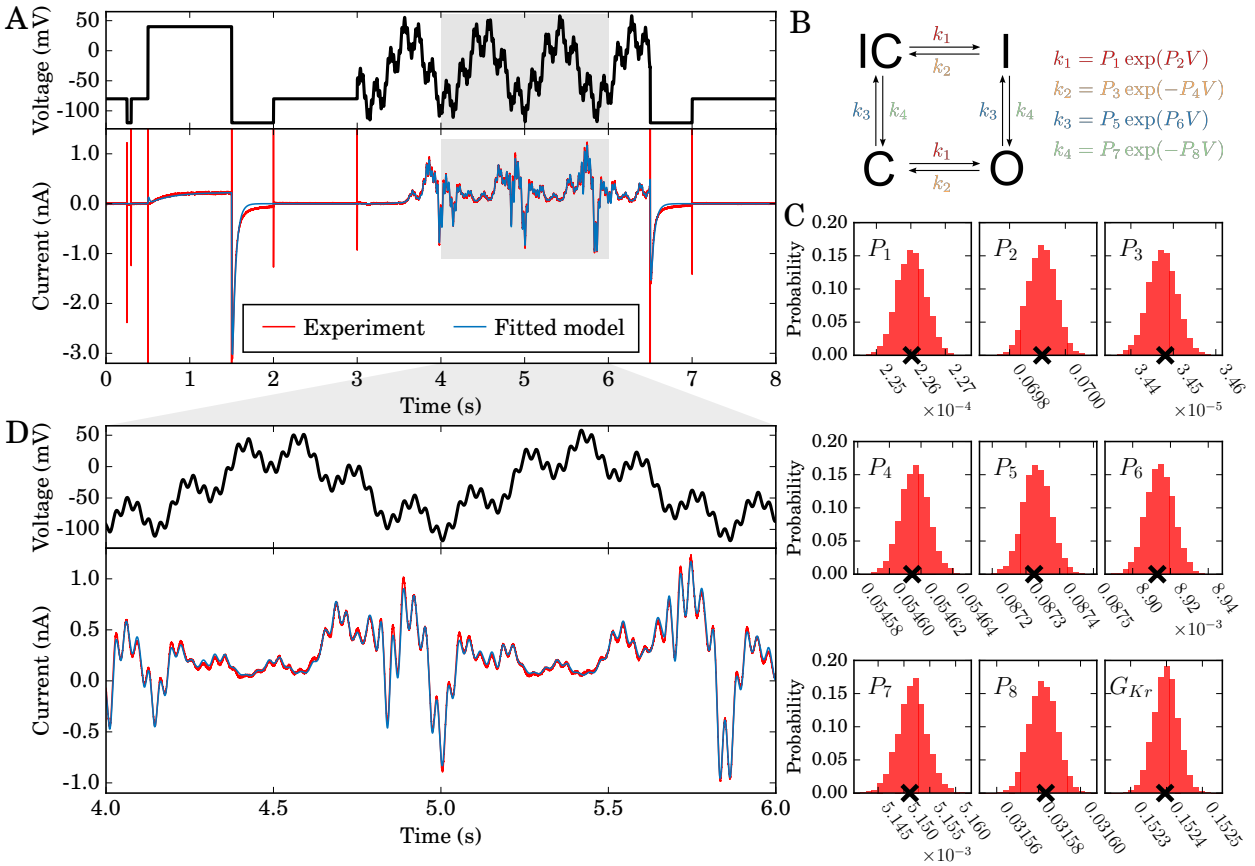

Figure 3: **Model calibration**. **A:** Top: the entire 8 second training protocol, bottom: an experimental recording with the fitted model simulation overlaid (portion of the sinusoid enlarged in panel D). This simulation uses the maximum posterior density parameter set, denoted with crosses in panel C. **B:** The model structure in Markov state diagram format, note that the symmetric transition rates mean this is equivalent to a Hodgkin & Huxley[20]-style model with two independent gates. Parameter values P_1 to P_8 define voltage (V)-dependent transitions (k) between conformational states. **C:** posterior distribution of single-cell derived model parameters. Probability density distributions are shown for each parameter after fitting to the experimental data shown in panel A. The parameter numbering corresponds to that shown in panel B. Crosses indicate the parameter set with the maximum posterior density. The standard deviation of each of these distributions is less than 0.2% of the maximum posterior density value. **D:** an enlargement of the highlighted region of panel A.

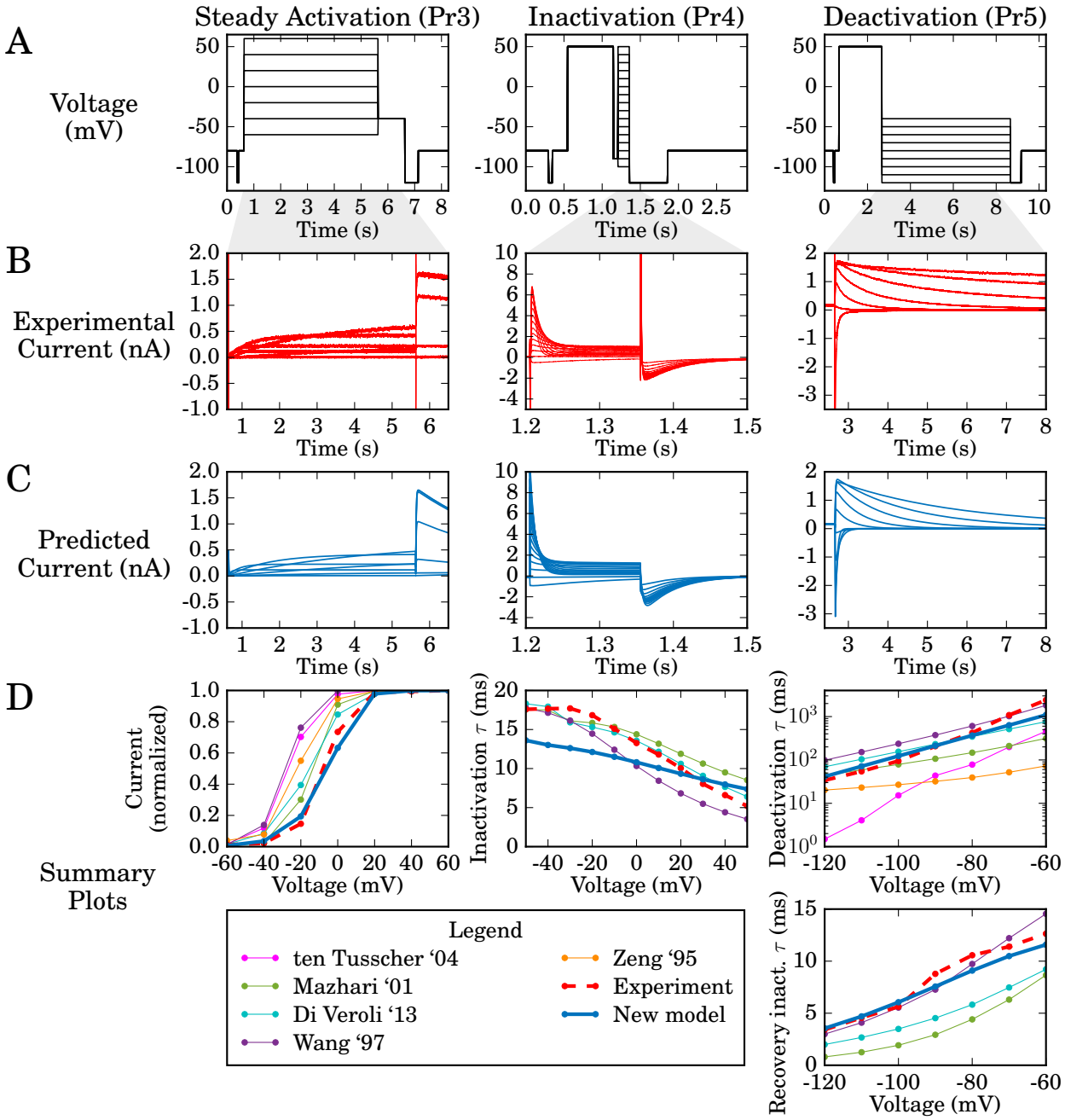

Figure 4: **Validation predictions — currents in response to traditional voltage step protocols**. Each column of graphs corresponds to a validation step protocol: those commonly used to study steady state activation, inactivation and deactivation (Pr3, Pr4, Pr5 in Figure 2) respectively. **A:** the voltage protocols. **B:** experimental current traces. **C:** model response — all are predictions using the maximum posterior density parameter set indicated in Figure 3C calibrated to just the sinusoidal protocol. **D:** summary curves, either current–voltage (I–V) or time constant–voltage (τ-V) relationships. These plots summarize the results in the relevant column. The model prediction is shown in blue bold throughout, and the experimental recording with a dashed red line. Note that the deactivation time constant we plot here is a weighted tau, described in Methods B1.7. Note that some literature model predictions are missing from the summary plots as we were either unable to fit exponential curves to 'flat' simulation output reliably; or the exponential decay occurred in the opposite direction to experimental traces, and we considered the comparison unwarranted.

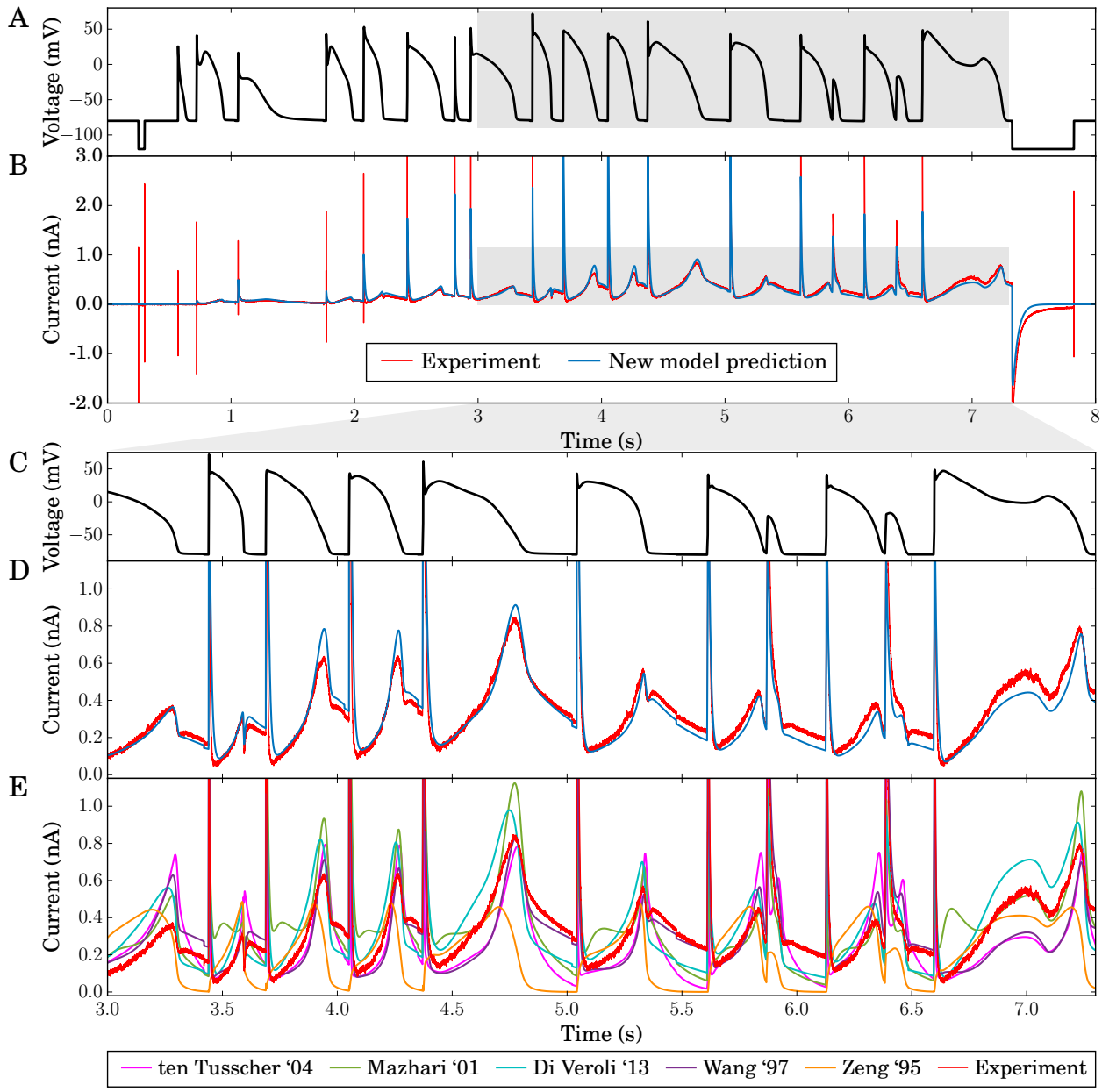

Figure 5: **Validation prediction — the current in response to the action potential protocol**. **A:** the voltage clamp protocol. **B:** a comparison of the experimental recording (red) and new model prediction (blue). **C & D:** enlargements of the highlighted regions of panels A & B. **E:** the same view of the experimental data in panel D, but here compared with predictions from literature I_{Kr} models. Conductance, G_{Kr}, is scaled for each of the literature models to give the least square difference between their prediction and these experimental data, i.e. we display a best-case scaling for each of these models. A quantification of the error in our model prediction versus these literature models is given in Supplementary Table D6: the performance shown in panels D and E holds for the whole trace, so the mean error in predicted current across the whole protocol is between 69% and 264% larger for the literature models' predictions than for our sine-wave fitted model.

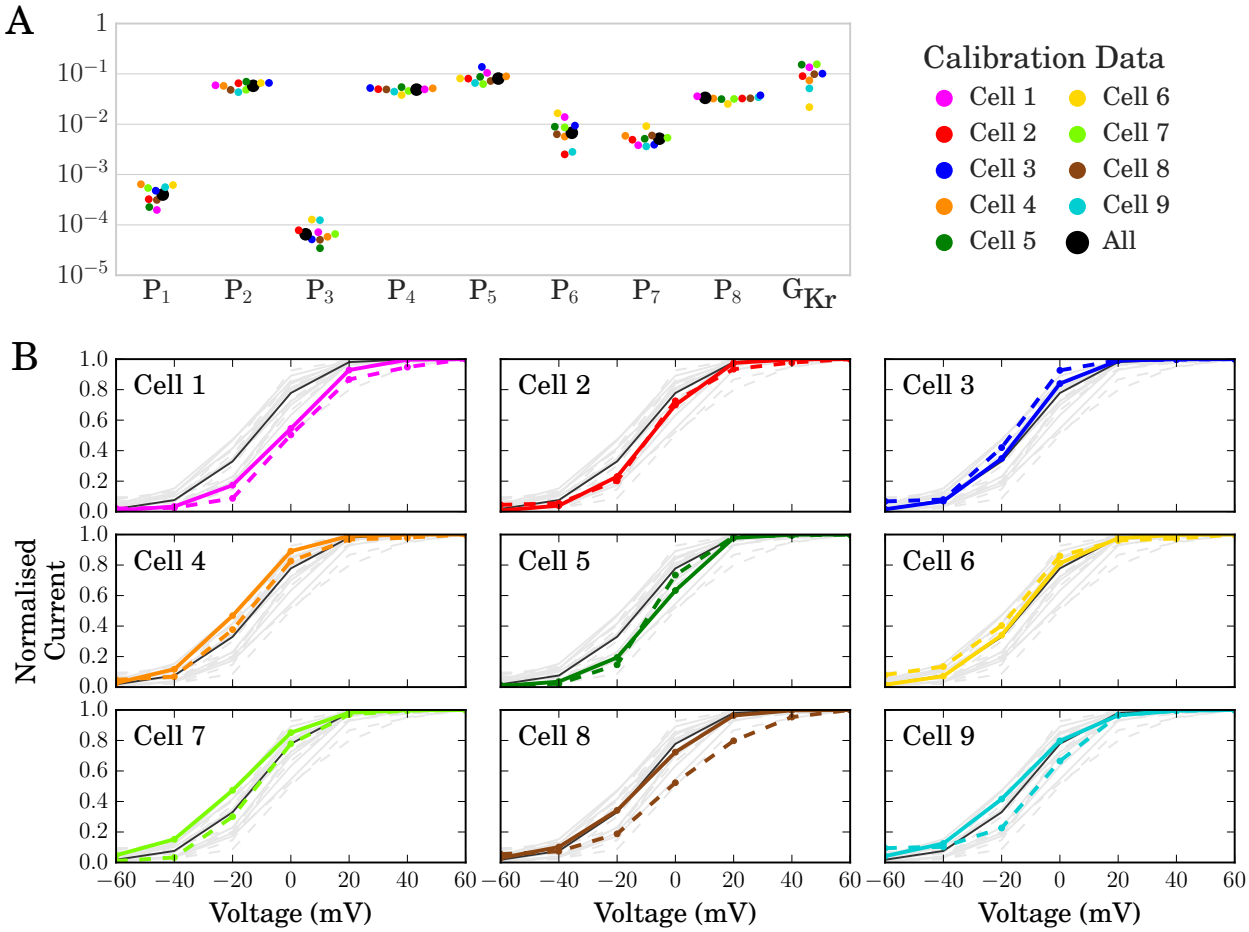

Figure 6: **Cell-specific model parameters, and comparison of their predictions with cell-specific experimental results**. (**A:**) Plot of parameters (maximum posterior density values) for nine cells obtained from training the model to the sinusoidal voltage protocol recorded on nine different cells, together with parameters calibrated to average data (N.B. not the average of the cell-specific parameters). The full set of parameter values are shown in Online Supplement Table F11 and the distributions for each parameter shown in Figure F11. (**B:**) Comparison of cell-specific model predictions to cell-specific experimental recordings for the steady-state peak current I–V curves from Pr3. Each plot represents a different cell, model predictions are depicted by a bold colored line, and dashed lines show values derived from the experimental data. The black lines (same on each plot) represent the prediction from the model calibrated to averaged sinusoidal data (all of the cells' data). Each subplot contains all of the other cells' recordings and predictions in light grey in the background to aid comparison and show the spread that we observed.

Sinusoidal voltage protocols for rapid characterization of ion channel kinetics: Online Supplement

Kylie A. Beattie Ph.D.[1,2], Adam P. Hill Ph.D.[3,4], Rémi Bardenet Ph.D.[5], Yi Cui Ph.D.[6], Jamie I. Vandenberg Ph.D.[3,4], David J. Gavaghan Ph.D.[1], Teun P. de Boer Ph.D.[7], Gary R. Mirams Ph.D.[8]

September 29, 2017

A Details of Published hERG Channel Models

Figure 1A of the main text features simulations from 29 literature hERG or I_{Kr} models. In Table A1 we list these models, give references, and show the seven different structures that they feature in Figure A1.

There are two models in this table that are not in Figure 1A: the Kiehn *et al.*[1] model as it is defined only at certain voltages; and the Piper *et al.*[2] model as it does not easily fit into the Hodgkin-Huxley/Markov model framework we used in our simulation code.

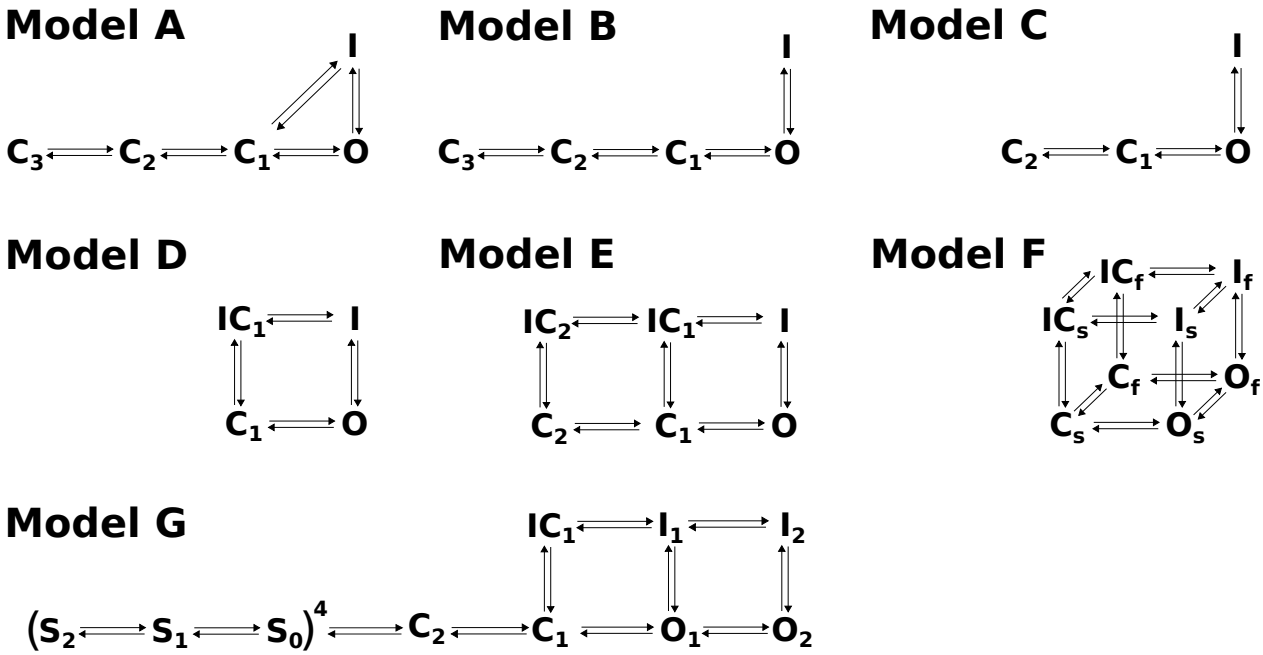

Figure A1: Different mathematical model structures for the literature models listed in Table A1. The model we use in the main text takes structure D as shown in Figure 3B. Note that, depending on their parameterisations, models D, E, F and G could satisfy independent gating (Hodgkin-Huxley assumptions) and then the states annotated as 'I' could also be considered 'IO' — but as drawn here this is not a requirement, and in neither case does current flow, so we removed the 'O' from these for simplicity.

Table A1: Table summarizing details of each published I_{Kr} model formulation, in chronological order. '*# Params*' indicates the total number of free parameters (the number given includes a G_{Kr} parameter for the conductance). The *Model Type* is 'HH' for Hodgkin–Huxley models and 'MM' for Markov Models, or a hybrid of the two (MM/HH, which generally means a MM with some symmetry in transition rates).

Model	Model Type	# Params	Experimental Cell Type	Temperature	Structure in Figure A1
Zeng *et al.*[3]	HH	11	Guinea pig ventricular myocytes	Physiological	D
Lindblad *et al.*[4]	HH	11	Rabbit SA, AV, atrial myocytes and rabbit and guinea pig ventricular myocytes	Physiological	D
Liu *et al.*[5]	MM	11	Ferret atrial myocytes	Room	C
Wang *et al.*[6]	MM	15	*Xenopus* oocytes	Room	B
Courtemanche *et al.*[7]	HH	10	Human atrial myocytes	Physiological	D
Nygren *et al.*[8]	HH	9	Human atrial/rabbit atrial myocytes and *Xenopus* oocytes	Physiological	D
Priebe & Beuckelmann[9]	HH	9	Human ventricular myocytes	Physiological	D
Kiehn *et al.*[1]	MM	9*	*Xenopus* oocytes	Room	A
Winslow *et al.*[10]	HH	7	Guinea pig ventricular myocytes	Physiological	D
Ramirez *et al.*[11]	HH	13	Canine atrial myocytes	Physiological	D
Zhang *et al.*[12]	HH	15	Rabbit sino-atrial node cells	Physiological	F
Clancy & Rudy[13]	MM	14	Guinea pig ventricular	Physiological	A
Lu *et al.*[14]	MM	17	Chinese Hamster Ovary (CHO)	Physiological	A
Mazhari *et al.*[15]	MM	17	Human Embryonic Kidney (HEK) 293	Physiological	A
Fox *et al.*[16]	HH	10	Canine ventricular myocytes	Physiological	D
Kurata *et al.*[17]	HH	18	Rabbit sino-atrial node cells	Physiological	F
Oehmen *et al.*[18]	MM	11	Rabbit sino-atrial cells	Physiological	C
Matsuoka *et al.*[19]	HH	23	Rabbit pacemaker and guinea pig ventricular myocytes	Physiological	F
Piper *et al.*[2]	MM/HH	43	*Xenopus* oocytes	Room	G
Seemann *et al.*[20]	HH	7	Human ventricular myocytes	Physiological	D
Hund & Rudy[21]	HH	11	Canine ventricular myocytes	Physiological	D
Shannon *et al.*[22]	HH	11	Rabbit ventricular myocytes	Physiological	D
ten Tusscher *et al.*[23]	HH	13	HEK 293/CHO/*Xenopus* oocytes	Physiological	D
Fink *et al.*[24]	MM	15	Human Embryonic Kidney (HEK) 293	Physiological	B
Aslanidi *et al.*[25]	HH	8	Canine Purkinje cells	Physiological	D
Inada *et al.*[26]	HH	20	Rabbit atrio-ventricular node cells	Physiological	F
Grandi *et al.*[27]	HH	12	Human ventricular myocytes	Physiological	D
O'Hara *et al.*[28]	HH	19	Human ventricular myocytes	Physiological	F
Severi *et al.*[29]	HH	17	Rabbit sino-atrial node cells	Physiological	F
Di Veroli *et al.*[30]	MM/HH	13	Chinese Hamster Ovary (CHO)	Room	E
Di Veroli *et al.*[30]	HH	17	Human Embryonic Kidney (HEK293) expressing canine ERG	Physiological	D

* The transition rates of the Kiehn *et al.*[1] model are defined at specific voltages, so for this model there are 8 parameters (and 1 conductance parameter) for each voltage at which the model is defined.

B Additional Methods

This section contains further description of the methods that were used, with a particular focus on details of the Bayesian Inference scheme in Section B2. These sections do not feature in the main Methods section due to space constraints.

B1 Additional Experimental Methods

B1.1 Cell Culture

Chinese Hamster Ovary (CHO) cells stably expressing Kv11.1 were used in the patch clamp experiments performed in this study. Cells were cultured in Ham's F12 nutrient mix containing 5% fetal bovine serum and maintained at 37°C with 5% CO_2.

B1.2 Electrophysiology Solutions

The bath solution was composed of: NaCl (137 mM), KCl (4 mM), $MgCl_2$ (1 mM), HEPES (10 mM), glucose (10 mM), and $CaCl_2$ (1.8 mM). The pH of the solution was adjusted to 7.4 with NaOH. Borosilicate glass micropipettes were pulled and fire polished to final tip resistances of approximately 2–5 MΩ when filled with pipette solution containing: KCl (130 mM), $MgCl_2$ (1 mM), HEPES (10 mM), EGTA (5 mM), and MgATP (5 mM). pH of the solution was adjusted to 7.2 with KOH. All experiments were performed at room temperature (21–22°C). Using this temperature and the composition of the bath and pipette solutions, a K^+ reversal potential of approximately -88.4 mV was calculated using the Nernst potential (equation (8)), the exact value depending on the particular temperature of each experimental recording.

B1.3 Recording Techniques

Current recordings were made using an Axopatch 200B amplifier in whole-cell patch clamp mode. Data acquisition was performed using pClamp 10 software (Molecular Devices, Sunnyvale, USA). The protocols were first created as text files and then converted to `.abf` stimulus files to make corresponding `.pro` protocol files in the pClamp 10 software. A CV 203BU amplifier headstage and a Digidata 1440A were used. A Sutter MP225 micromanipulator was used for positioning of the microelectrode. The current signal was sampled at a rate of 10 kHz. 75–80% series resistance compensation was applied and data were 5 kHz low pass Bessel filtered by the hardware. No software filtering was applied. Whole-cell capacitance compensation was applied electronically. Leak subtraction was applied offline by using a 50 ms leak step to allow correction. To make a series of successive recordings using different protocols on the same cell, the pClamp "Sequencing Keys" tool was utilized, with a `.sks` file detailing the sequence the protocols should be performed in.

B1.4 Details of Voltage Clamp Protocols

Here we list the details of the voltage-clamp protocols that were not included in the main text. The protocols can also be found encoded in the software, available to download as described at the end of the main text.

Protocol 0 — Repeated activation step

Before the start of each set of recordings on each cell an activation step protocol with a start-to-start interval of 12 seconds was repeated several times until consistent currents were observed on each

repeat. From an initial holding potential of −80 mV, this protocol comprised a 5 s step to 10 mV followed by a 5 s step to −50 mV before returning again to a holding potential of −80 mV. This protocol is depicted in Supplementary Figure B2. We repeated this protocol while dofetilide was added (see Figure 1B) and the current traces recorded from this protocol were used to assess when a steady level of dofetilide block had been reached.

Protocols 1,2 — Activation Kinetics

After the initial period at holding potential incorporating the −120 mV leak step, a step to V_{step_1} followed and was held at that voltage for T_{step} ms, before a step to −120 mV for 2.5 s, before returning to holding potential of −80 mV for 1 second. The protocol was repeated 6 times with a different T_{step} on each repeat. T_{step} took the values of 3, 10, 30, 100, 300 and 1000 ms.

- For Protocol 1, V_{step_1} is 0 mV. This protocol is depicted in Supplementary Figure B3.
- For Protocol 2, V_{step_1} is +40 mV. This protocol is depicted in Supplementary Figure B4.

Figures B2–B4 show plots of the voltage clamps that are used in the repeated activation step and activation kinetics protocols (Pr0–Pr2).

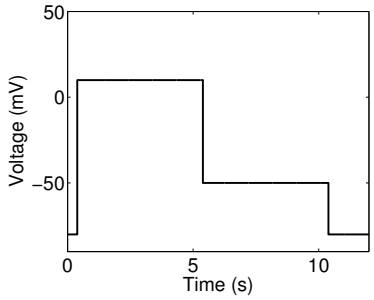

Figure B2: Repeated Activation Step Protocol (Pr0).

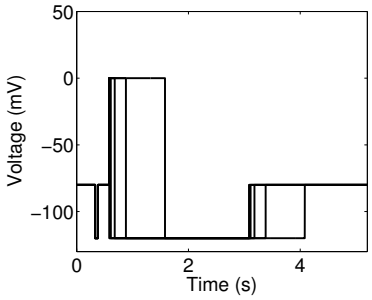

Figure B3: Activation Kinetics 1 Protocol (Pr1).

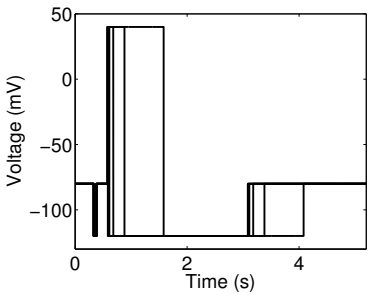

Figure B4: Activation Kinetics 2 Protocol (Pr2).

Protocol 3 — Steady-State Activation

From the initial period at holding potential incorporating the −120 mV leak step, a step to V_{step} was applied for 5 seconds, followed by a 1 s step to −40 mV, before a 500 ms step to −120 mV, and then returning back to holding potential for one second. This process was repeated 7 times with a different V_{step} on each repeat. V_{step} ranged from −60 mV to +60 mV in 20 mV increments. This protocol is depicted in Figure 4A (left column).

Protocol 4 — Inactivation

From the initial period at holding potential incorporating the −120 mV leak step, a step to 50 mV for 600 ms, and a step to −90 mV for 60 ms, followed by a step to V_{step} for 150 ms, before a 500 ms step to −120 mV, and a 1 s step back to holding potential of −80 mV; This was repeated 16 times with a different V_{step} on each repeat. V_{step} ranged from −100 mV to 50 mV in 10 mV increments. This protocol is depicted in Figure 4A (middle column).

Protocol 5 — Deactivation

From the initial period at holding potential incorporating the −120 mV leak step, a step to 50 mV for 2 s was applied, followed by a step to V_{step} for 6 s, before a 500 ms step to −120 mV, and then returning back to holding potential for one second. This process was repeated 9 times with a different V_{step} on each repeat. V_{step} ranged from −120 mV to −40 mV in 10 mV increments. This protocol is depicted in Figure 4A (right column).

Protocol 6 — Action Potentials Clamp

See main text.

Protocol 7 — Sinusoidal Clamp

The full protocol is comprised of 250 ms at holding potential of −80 mV, followed by a 50 ms 'leak detection' step to −120 mV, and then 200 ms back at −80 mV. This was followed by an 'activation' step of 1 s step to 40 mV; a 'closing' 500 ms step to −120 mV; and a return to −80 mV for 1 second. The 3.5 s sinusoidal portion of the protocol then followed (the form of which is described below), before a 'closing' 500 ms step to −120 mV, and a return to −80 mV for 1 s.

The sinusoidal portion of the protocol takes the form of a sum of three sine waves as discussed in the main text Equation (1), and repeated here for convenience:

$$V(t) = -30 + A_1 \sin(\omega_1(t - t_0)) + A_2 \sin(\omega_2(t - t_0)) + A_3 \sin(\omega_3(t - t_0)),$$

where $A_1 = 54\,\text{mV}$, $A_2 = 26\,\text{mV}$, $A_3 = 10\,\text{mV}$, $\omega_1 = 0.007\,\text{ms}^{-1}$, $\omega_2 = 0.037\,\text{ms}^{-1}$ and $\omega_3 = 0.19\,\text{ms}^{-1}$, and t is time measured in milliseconds.

The protocol was initially designed with just the −120 mV leak step and not the additional 'activation' steps to 40 mV and −120 mV (which were included after preliminary experiments as described in Section B2.2) and so the sine wave was shifted using $t_0 = 2500\,\text{ms}$ to begin at the same phase after we incorporated the additional steps. This offset is not expected to be important to include, but was included here for clarity for anyone attempting to reproduce our study.

B1.5 Liquid Junction Potential

All of the protocols described in this section were adjusted on the amplifier to account for the liquid junction potential which was calculated to be 4.1 mV from the ionic composition of our physiological solutions which are described in Section B1.2. The liquid junction potential was calculated using the junction potential calculator in the pClamp software.

B1.6 Effect of Dofetilide Subtraction

To show the effect of 0.3 μM dofetilide subtraction and to demonstrate the lack of endogenous currents remaining following this step, we compare the current traces before and after dofetilide subtraction in Figure B5. We show currents from Cell #5 which features in the figures of the main text.

There was little contribution from endogenous currents in these cells. The application of 0.3 μM dofetilide eliminates almost all current, indicating that both the vehicle recording and 'dofetilide subtracted' currents are almost entirely due to hERG. While levels of endogenous currents and the impact of leak subtraction on the current traces may vary from cell-to-cell, overall we found only small endogenous currents were observed in the cells.

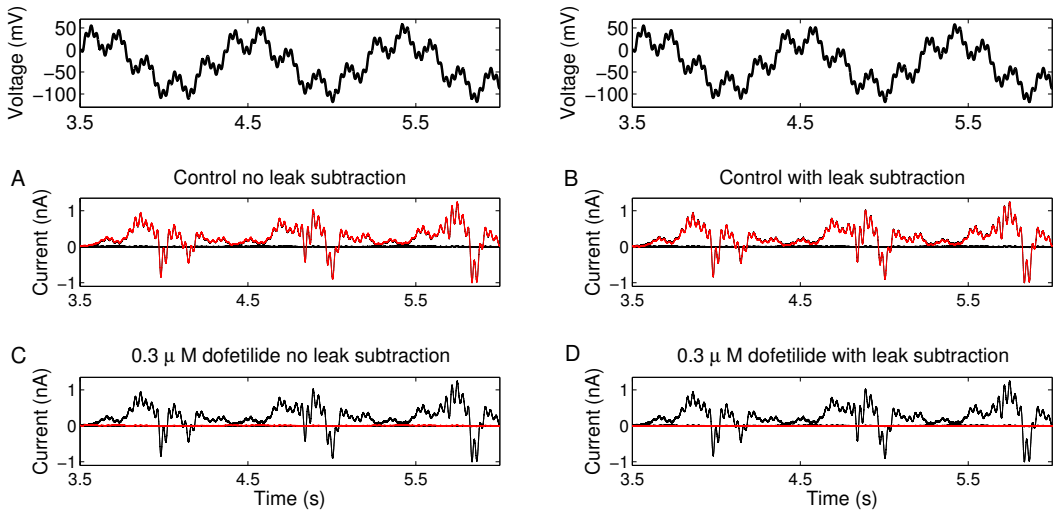

Figure B5: Raw recordings, recordings with leak subtraction, and 0.3 μM dofetilide controls for Cell #5. Top row: input voltage trace from the sine wave protocol (same on both sides for comparison with traces below). In A–D we show the current in response to this voltage protocol in four situations — each panel shows the same four traces, with a different one highlighted in red. In A we highlight the raw recording of whole current; in B the whole current recording after leak subtraction, in C the raw recording after the addition of dofetilide; and in D the dofetilide recording after leak subtraction.

An example of where dofetilide subtraction may play a more important role is shown in Figure B6, where the hERG current is much lower and so any contribution from endogenous currents would have more impact and it may be important to remove this contribution. This example is for Cell #6 from the main text.

B1.7 Deriving IV Curves and Time Constant-V Curves

To derive time constant-voltage relationships from experimental data and simulated data traces, we used the Levenberg-Marquardt algorithm with a tolerance of 10^{-6} within Clampfit v10.5. To derive the instantaneous inactivation time constant curves shown in Figure 4 (inactivation column, row D) we fitted a single a single exponential to the current responses during the 150 ms V_{step}, as defined in the inactivation protocol (Pr4) description above.

To produce the deactivation and recovery from inactivation rate time constant–voltage relationship for the experimental data traces, we fitted a triple exponential through the experimental data trace from the deactivation protocol (Pr 5). The section of the data used for fitting is the current in response to the 6 second V_{step}. Both this region of experimental data used for fitting and that for the instantaneous inactivation time constant described above are highlighted in row B of Figure 4. The fastest time constant from the triple exponential fit to each test step corresponded to the recovery from inactivation time constant. We then used the weights of the remaining two time constants from each triple exponential fit to produce a single weighted time constant for deactivation[31]. To derive the deactivation and recovery from inactivation time constants from simulated data we fitted a double exponential through the current in response to the 6 second V_{step} section of the

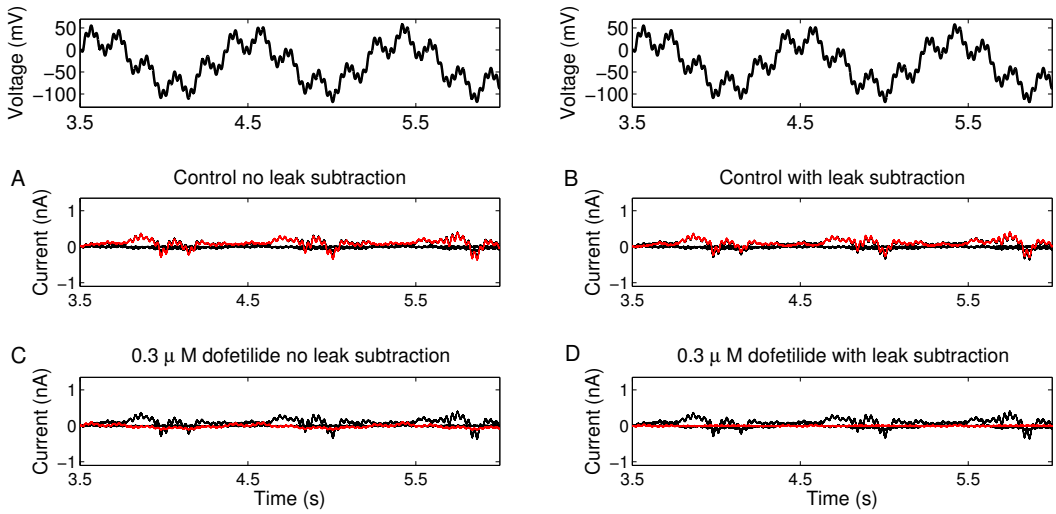

Figure B6: Raw recordings, recordings with leak subtraction, and 0.3 μM dofetilide controls for Cell #6. Top row: input voltage trace from the sine wave protocol (same on both sides for comparison with traces below). In A–D we show the current in response to this voltage protocol in four situations — each panel shows the same four traces, with a different one highlighted in red. In A we highlight the raw recording of whole current; in B the whole current recording after leak subtraction, in C the raw recording after the addition of dofetilide; and in D the dofetilide recording after leak subtraction.

deactivation protocol. Again, we used the faster time constant as the recovery from inactivation time constant and the slower time constant as that for deactivation.

To produce the peak current-voltage relationship for the steady state activation protocol for the simulated data traces we wrote MatLab code to identify the peak current in the region between 5.6292 and 5.7292 seconds on each sweep of the protocol, which corresponds to the current response just after the 5 second V_{step} when the voltage is stepped to -40 mV. We then normalized the peak current data to the maximum overall peak identified in this region to produce the current-voltage relationship curve. For the simulated data we wrote a MatLab script (included in code download) to identify the peak-current voltage relationship for this protocol but for the experimental traces we verified these peak points manually to avoid incorrect peaks being identified due to noise or capacitive effects. We also identified the peak currents in the currents evoked by the activation kinetics protocols manually for the same reason. In the activation kinetics protocol we identified the peak currents during the V_{step} for each interval of T_{step} duration.

B2 Bayesian Inference Scheme

B2.1 Likelihood formulation

For an observed experimental recording which we will denote $\mathbf{y}$, we can infer the probability of different combinations of model parameters θ. Bayes' rule underpins this approach which is expressed as

$$P(\theta|\mathbf{y}) = \frac{P(\mathbf{y}|\theta)P(\theta)}{P(\mathbf{y})} \tag{B.1}$$

$P(\theta|\mathbf{y})$ is a probability density that encodes our belief that the parameters of the model are in a neighborhood of θ after observing the experimental data $\mathbf{y}$, and is termed the *posterior probability density*. $P(\mathbf{y}|\theta)$ is the probability density that corresponds to the probabilistic generation of the experimental data $\mathbf{y}$ given a model parameterized with parameters θ. $P(\theta)$ encapsulates our beliefs about θ before observing any experimental data and is termed the *prior distribution* (details of the prior that we used are in Online Supplement B2.3). $P(\mathbf{y})$ is a normalizing term which is the integral of all possible probabilities $P(\mathbf{y}|\theta)$ and ensures that the posterior density $P(\theta|\mathbf{y})$ integrates to 1. In practice this normalizing term is calculated by

$$P(\mathbf{y}) = \int P(\mathbf{y}|\theta)P(\theta)\mathrm{d}\theta. \tag{B.2}$$

A Bayesian inference approach to parameter estimation combines beliefs about the parameters in the prior distribution $P(\theta)$ with the *likelihood* $P(\mathbf{y}|\theta)$ to determine the posterior probability distribution $P(\theta|\mathbf{y})$.

We define the likelihood

$$L(\theta|\mathbf{y}) = P(\mathbf{y}|\theta) \tag{B.3}$$

to insist on the fact that we consider it as a function of θ, with $\mathbf{y}$ kept fixed at the observation values. Bayes' rule (in Equation (B.1)) can be rewritten in terms of likelihood as

$$P(\theta|\mathbf{y}) \propto P(\theta)L(\theta|\mathbf{y}). \tag{B.4}$$

When the prior distribution is assumed to be uniform (as it is in this study), we can make inferences based on just the likelihood, as the prior $P(\theta)$ is either constant or zero. If a proposed parameter is outside our chosen prior then likelihood is 0 and we simply record that this parameter set has a likelihood of 0 and propose another parameter set.

We assume that the errors at each time point are independent and so the conditional probability density of observing the whole experimental trace from time sample 0 to time sample T given the model parameter set θ is

$$L(\theta|\mathbf{y}) = \prod_{t=0}^{T} P(y_t|\theta). \tag{B.5}$$

We assume that the experimental noise is independently and normally distributed with a mean of zero and variance of σ^2. The likelihood is then expressed as

$$L(\theta|\mathbf{y}) = \prod_{t=0}^{T} \mathcal{N}(y_t|f_t(\theta), \sigma^2) = \prod_{t=0}^{T} \frac{1}{\sqrt{2\pi\sigma^2}} \exp\left(-\frac{(y_t - f_t(\theta))^2}{2\sigma^2}\right). \tag{B.6}$$

In our case $f_t(\theta)$ is the predicted current at each time point given the parameters, this is given by equation (7) after solving the model system (equations (3)–(6)). Calculating equation (B.6) requires the evaluation of the product of many numbers less than 1, so it is more numerically convenient to calculate the *log-likelihood* instead. As our aim is to identify parameter sets θ which maximize the likelihood in equation (B.6), maximizing the likelihood is equivalent to maximizing the log-likelihood:

$$\log\left(L(\theta|\mathbf{y})\right) = -\frac{1}{2}\sum_{t=0}^{T} \log(2\pi\sigma^2) - \frac{1}{2}\sum_{t=0}^{T} \frac{(y_t - f_t(\theta))^2}{\sigma^2}. \tag{B.7}$$

In practice, the sums over time in equation (B.7) are formulated so that we exclude time points from regions where the data are affected by capacitive spikes. To be precise, we exclude 5 ms

intervals following step-changes in the imposed voltage clamp. In the sine wave protocol (Pr7) these step-changes occur at 0.25 seconds, 0.3 seconds, 0.5 seconds, 1.5 seconds, 2 seconds, 3 seconds, 6.5 seconds and 7 seconds (spikes are seen in experimental recordings at these times in Figure 2).

B2.2 Conductance estimation to inform the prior

Preliminary work revealed that using sine wave protocols alone often allowed kinetic parameters in the hERG model to be recovered, but there was potential for identifiability problems (or at least we encountered difficulties in finding a global optimum due to a rugged likelihood surface) when simultaneously fitting the conductance parameter and transition rate parameters P_1 to P_8 (although previous work suggests all parameters are theoretically identifiable[32]). To add extra information on conductance, we incorporated a voltage-step to $+40\,\mathrm{mV}$ followed by a step down to $-120\,\mathrm{mV}$, as described in the definition of the sinusoidal protocol above. The aim being to provoke a large current. We then fitted a single exponential through the slow time constant of the tail current exhibited during the $-120\,\mathrm{mV}$ step (fitting was performed in the Clampfit software, using the Levenberg-Marquardt algorithm with a tolerance of 10^{-6}). We then extrapolated back to the point at which the voltage step to $-120\,\mathrm{mV}$ was made, and used the extrapolated current value at this point to estimate a conductance at this time point (this extrapolation method is described in Vandenberg *et al.*[33]). The conductance we estimated was used as a lower bound for the prior distribution of the conductance, as we describe below.

B2.3 Prior

In this section we describe our prior assumptions on the values that each model parameter can take. The prior for the conductance G_{Kr} is assumed to be independent of the kinetic parameters, and to take a uniform distribution. As discussed above, the lower bound is formed by estimating a lower bound on the conductance value 'directly' from the experimental data; the upper bound is assumed to be 10 times the value of the lower bound.

The other model parameters are within transition rates of the form

$$k = A\exp(BV), \tag{B.8}$$

where V is voltage and A and B are model parameters (P_1 to P_8 for k_1 to k_4, as shown in Figure 3).

For parameters of the form A we assumed that the prior distribution is uniform between 10^{-7} and $1000\,\mathrm{ms}^{-1}$, again to cover (and extend beyond) the full physiological range expected with hERG channel gating.

We assume that the prior distributions for B parameters are uniform between 10^{-7} and 0.4 mV^{-1}. The lower bound for this parameter was selected as the voltage-dependence becomes practically redundant when B becomes small: when $B = 10^{-7}$ the value of $\exp(BV)$ will change by less than 0.0015% across the voltages we reach in this study. The upper value is beyond the physiologically expected range.

We also impose a prior on the maximum rate of transition k between any states (maximum across the full voltage range in the protocol (that is from -120 to 58.25 mV)). If the maximum rate k is greater than $1000\,\mathrm{ms}^{-1}$, or less than $1.67 \times 10^{-5}\,\mathrm{ms}^{-1}$, the pair of parameter values that give rise to this are assigned prior probability zero (strictly, this is equivalent to defining 2D prior on A and B, but is easier to describe here, and code, as an additional constraint): the lower bound is based on the assumption that a transition is not physiologically realistic if it occurs over a time scale slower than one minute; the upper bound was decided based on the prior for the individual

parameters A and B in the transition rate expression and to prevent the transitions occurring over a time scale much faster than would be physiologically expected.

Note that our analysis is relatively insensitive to the precise form of the prior that is used as there are around 80,000 data points (8 s of 10 kHz samples) in the likelihood product calculation of Equation (B.5), which is then also in a product with the prior in Equation (B.4). So, effectively, each of the 10,000 data points has the same impact as the prior does on the posterior. Given our likelihood is extremely peaked around its maximum (Figure 3C), we have observed no notable influence of the shape of the prior, as long as the maximum posterior density point is well away from the limits described above — which it has been in all cases. Note that the same concept means that, in our case, the "maximum likelihood estimate" (MLE — parameter set that maximizes Equation (B.5)) would be practically indistinguishable from the "maximum a posteriori estimator" (MAP — parameter set that maximizes Equation (B.4)) even if we had a non-uniform prior.

B2.4 Global minimization

The Covariance Matrix Adaptation — Evolution Strategy (CMA-ES) algorithm was used to perform an initial exploration of the surface of the posterior density, and to identify parameter sets which allow the model to fit the experimental data well. The tolerance used is 10^{-4} and all other settings are the defaults in MatLab implementation of CMA-ES v3.61, downloaded from `https://www.lri.fr/~hansen/cmaes.m`. We imposed bounds based on the prior as we describe above in Section B2.3.

We run the CMA-ES algorithm from different starting points and continue to do so until we identify the same region of parameter space for optimal parameter sets for each experimental data trace when starting from many different starting points. In this way, we can be confident that we identify the same region of high likelihood consistently (not simply the first local minimum that is found), and we have more confidence that this corresponds to the globally optimal likelihood.

These initial starting points for the CMA-ES algorithm are sampled from within the prior defined for each parameter, described in section B2.3. To sample from the prior we simply select the voltage-dependent transition rate parameters (of the form B described above) uniformly from the defined range. The same approach is used to sample the conductance parameter.

For the parameters of the form A above we sample starting points in a logarithmic fashion across the range of the uniform prior. This approach helps to restrict the initial guesses of parameters to the region of measurable time scales we imposed by defining the maximum and minimum ranges on the overall transition rate, as described above. We also run a small selection of starting points with both A and B parameter values sampled uniformly from $[10^{-7}, 0.1]$ (the range in which most existing model parameters lie), again to ensure we identify the global optimal solution to the optimization problem. We log-transform all parameters within CMA-ES to aid the optimization process by making all values similar orders of magnitude.

B2.5 Markov Chain Monte Carlo parameter inference

We use *Markov Chain Monte Carlo* (MCMC) methods to explore the posterior probability distribution. The approach we use is the *Metropolis-Hastings* algorithm. In this algorithm, candidate parameter sets are proposed from a *proposal distribution* $q(\theta_{\mathbf{cand}}|\theta_{\mathbf{i}})$ which depends only on the previously accepted parameter set $\theta_{\mathbf{i}}$. We use a multivariate normal distribution as our proposal distribution. Any candidate parameter set θ_{cand} is compared to the current parameter set θ_i by calculating the ratio of the likelihood of the two parameter sets. The value of the ratio determines whether or not the proposed parameter set is accepted as part of the MCMC chain. If the candidate parameter set has a greater posterior density value than the existing parameter set then

it will be added to the Markov chain, that is $\theta_{\mathbf{i+1}} = \theta_{\mathbf{cand}}$. Otherwise, the parameter set may still be accepted with a probability equal to the ratio of likelihood/posterior density values. That is, a proposed parameter set generated from a multivariate normal distribution is accepted with probability

$$\alpha = \min\left\{\frac{L(\theta_{\mathbf{cand}}|\mathbf{y})}{L(\theta_{\mathbf{i}}|\mathbf{y})}, 1\right\}. \tag{B.9}$$

Also note that if the proposed parameter set contains any parameters outside the range of the prior, or violates any of the conditions on the parameters that we have imposed, the parameter set is assigned an acceptance probability of 0 and immediately rejected and the previously accepted parameter set is again added to the Markov chain — that is, $\theta_{i+1} = \theta_i$.

In practice, we use a covariance matrix adaptive version of the Metropolis-Hastings Algorithm which helps identify the directions in parameter space which have the highest likelihood values, the algorithm is described in Haario *et al.*[34]. At each iteration of the algorithm, the covariance matrix of the multivariate normal distribution is updated and a scalar value is also updated to define the width of the distribution. We run our MCMC chains for 250,000 samples and discard the first 50,000 samples as 'burn in' (for an introduction to MCMC see Gilks *et al.*[35]).

C Synthetic Data Study to Assess Protocol Information Content

In order to verify that there was sufficient information within the sinusoidal protocol to parameterize our model we performed a *synthetic data* study. The aim in such a study is to ascertain whether we can recover the parameters used in the simulation from a simulated data trace (with added noise in this case).

C1 Producing synthetic data

In order to produce synthetic data we simulate with some fixed known parameter set. We performed this with both our best initial parameter set estimate (those parameters in literature HH models), and also from the parameters we obtained after fitting to the experimental data trace as we present here (both showed good identifiability). We scale the simulated trace by multiplying by this factor, so it becomes approximately the same magnitude (in nA) as the experimental trace. We estimated the typical level of noise from the experimental trace by calculating the standard deviation σ of the experimental current during the first 200 ms (where the current is around zero at the initial holding potential of -80 mV). We then generate a synthetic data trace by adding normally distributed noise with a mean of zero and the standard deviation equal to the noise estimated from the experimental trace ($\sim N(0, \sigma^2)$) to the conductance-scaled simulated trace. The example we present here uses the experimental reference trace from Cell #5, featured in much of the manuscript.

C2 Inferring parameters from synthetic data

We then attempt to infer parameters from this synthetic data trace, using the CMA-ES algorithm followed by MCMC as described in Section 2.5. In Figure C7 we present probability density distributions obtained when using both synthetic and experimental traces. We are able to recover the original parameters underlying the synthetic trace with high accuracy.

The synthetic data study provides us with confidence in the suitability of our protocol for accurately identifying parameters of the model presented in Figure 3B in the main text, and also that the parameter inference protocol(s) we are using are suitable for the task. We believe such an approach should always be used to test whether there is sufficient information in the experimental data being proposed for calibration of a mathematical model. The test should be performed twice: before conducting the experiment (with the pre-existing best guess at the parameters); and also after conducting the experiment (with the new maximum posterior density estimate of the parameters — as we illustrate in Figure C7).

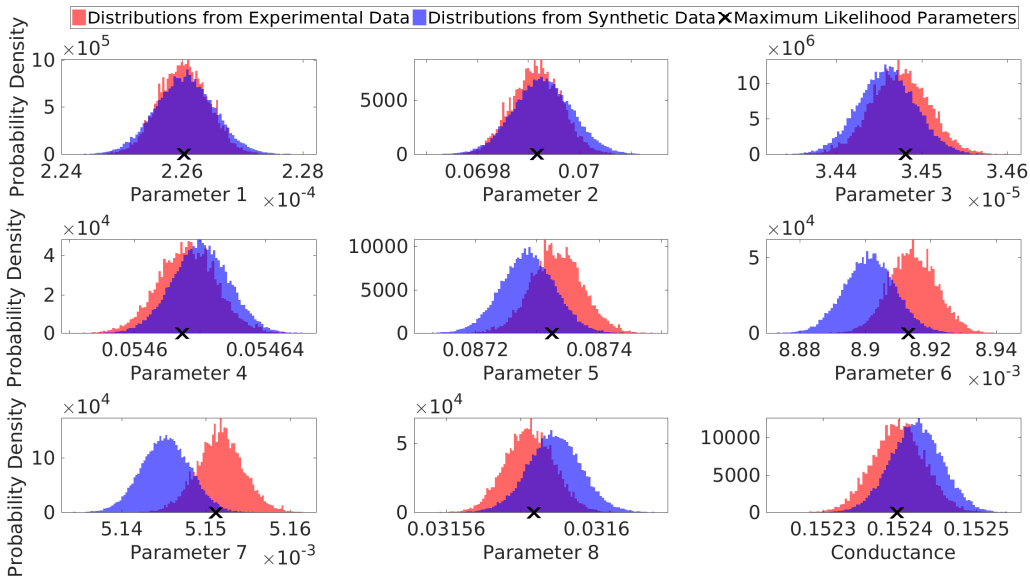

Figure C7: Probability density distributions for each parameter estimates from fitting to both experimental data (red) and simulated data (blue). Crosses indicate the parameter set with the maximum posterior density.

D Cell-Specific versus Literature Model Predictions

In Tables D2–D10 we compare the predictions given by each cell-specific model with a range of literature model predictions. We compare their ability to predict the full current traces for the validation protocols Pr3–6 discussed in the main text. Each table provides the mean (over each time point) square difference between an experimental current recording in one particular cell and its cell-specific model prediction under each of the validation protocols, and compares this with current predictions from a range of literature models. Equation (F.10) gives the formula that was used to calculate the error entries.

Note that we have to choose a conductance value, G_{Kr}, for the literature models. G_{Kr} is selected differently for each cell by minimizing the error metric for the predicted current trace under the action potential protocol (Pr6) for each model (a best-case scenario for each literature model). Our new cell-specific models' conductances were fitted to the sine wave protocol (Pr7), along with the rest of their parameters. N.B. the literature model predictions are worse if we scale them to fit the sine wave; we considered this perhaps unjustified since they were developed never having seen such a protocol.

Despite literature models having their conductance scaled to minimize error in the Pr6 (action potential clamp) current prediction; only the Di Veroli *et al.*[30] model for Cell #9 performs better than our cell-specific models. The sine-wave fitted model outperforms all other literature models for all other cells.

Additionally, the Wang *et al.*[6] model gives better predictions for the deactivation protocol current for some cells and for the steady state activation protocol for Cell #4. The Di Veroli *et al.*[30] model gives better predictions for the inactivation protocol for Cells #2, and #9; and the deactivation protocol for Cell #6. The Mazhari *et al.*[15] model gives a better prediction for the steady state activation protocol for Cell #7.

Table D2: Table quantifying mean square difference (units nA) between experimental current traces and simulation predictions for the validation protocols shown in Figures 4 and 5 for Cell #1. Here the color scale is set so that ■ represents zero error and ■ represents the highest error for each protocol/column.

Model	Sine Wave (Pr7)	AP (Pr6)	Steady Act. (Pr3)	Deact. (Pr5)	Inact. (Pr4)
New model for Cell #1	0.0151	0.0283	0.0332	0.0925	0.0312
Wang *et al.*[6]	0.0389	0.0419	0.0842	0.1195	0.0402
Di Veroli *et al.*[30]	0.0487	0.0545	0.0916	0.1400	0.0479
Mazhari *et al.*[15]	0.0499	0.0516	0.0731	0.1491	0.0564
ten Tusscher *et al.*[23]	0.0599	0.0557	0.0939	0.1538	0.0653
Zeng *et al.*[3]	0.0787	0.0802	0.0989	0.1616	0.0638

Table D3: Table quantifying mean square difference (units nA) between experimental current traces and simulation predictions for the validation protocols shown in Figures 4 and 5 for Cell #2. Here the color scale is set so that ■ represents zero error and ■ represents the highest error for each protocol/column.

Model	Sine Wave (Pr7)	AP (Pr6)	Steady Act. (Pr3)	Deact. (Pr5)	Inact. (Pr4)
New model for Cell #2	0.0164	0.0295	0.0270	0.0656	0.0219
Wang *et al.*[6]	0.0529	0.0528	0.0746	0.0633	0.0384
Di Veroli *et al.*[30]	0.0314	0.0302	0.0506	0.0679	0.0212
Mazhari *et al.*[15]	0.0361	0.0380	0.0533	0.0939	0.0324
ten Tusscher *et al.*[23]	0.0575	0.0639	0.0846	0.1011	0.0539
Zeng *et al.*[3]	0.0654	0.0717	0.0828	0.1070	0.0452

Table D4: Table quantifying mean square difference (units nA) between experimental current traces and simulation predictions for the validation protocols shown in Figures 4 and 5 for Cell #3. Here the color scale is set so that ■ represents zero error and ■ represents the highest error for each protocol/column.

Model	Sine Wave (Pr7)	AP (Pr6)	Steady Act. (Pr3)	Deact. (Pr5)	Inact. (Pr4)
New model for Cell #3	0.0253	0.0415	0.0658	0.0785	0.0537
Wang *et al.*[6]	0.0472	0.0492	0.0729	0.0648	0.0549
Di Veroli *et al.*[30]	0.0630	0.0859	0.1136	0.1034	0.0743
Mazhari *et al.*[15]	0.0627	0.0819	0.0910	0.1099	0.0835
ten Tusscher *et al.*[23]	0.0733	0.0712	0.0936	0.1101	0.0822
Zeng *et al.*[3]	0.0972	0.1153	0.1216	0.1282	0.0868

Table D5: Table quantifying mean square difference (units nA) between experimental current traces and simulation predictions for the validation protocols shown in Figures 4 and 5 for Cell #4. Here the color scale is set so that represents zero error and represents the highest error for each protocol/column.

Model	Sine Wave (Pr7)	AP (Pr6)	Steady Act. (Pr3)	Deact. (Pr5)	Inact. (Pr4)
New model for Cell #4	0.0258	0.0359	0.0701	0.0878	0.0522
Wang *et al.*[6]	0.0595	0.0443	0.0587	0.0506	0.0537
Di Veroli *et al.*[30]	0.0429	0.0559	0.1045	0.0955	0.0596
Mazhari *et al.*[15]	0.0472	0.0581	0.0709	0.1074	0.0681
ten Tusscher *et al.*[23]	0.0668	0.0741	0.0760	0.1030	0.0665
Zeng *et al.*[3]	0.0832	0.1067	0.1079	0.1282	0.0733

Table D6: Table quantifying mean square difference (units nA) between experimental current traces and simulation predictions for the validation protocols shown in Figures 4 and 5 for Cell #5. Here the color scale is set so that represents zero error and represents the highest error for each protocol/column.

Model	Sine Wave (Pr7)	AP (Pr6)	Steady Act. (Pr3)	Deact. (Pr5)	Inact. (Pr4)
New model for Cell #5	0.0203	0.0453	0.0437	0.1317	0.0700
Wang *et al.*[6]	0.0725	0.0764	0.1374	0.1611	0.0933
Di Veroli *et al.*[30]	0.0675	0.0958	0.1148	0.1881	0.0735
Mazhari *et al.*[15]	0.0824	0.0963	0.1009	0.2286	0.1012
ten Tusscher *et al.*[23]	0.1080	0.1260	0.1603	0.2422	0.1415
Zeng *et al.*[3]	0.1318	0.1650	0.1620	0.2575	0.1259

Table D7: Table quantifying mean square difference (units nA) between experimental current traces and simulation predictions for the validation protocols shown in Figures 4 and 5 for Cell #6. Here the color scale is set so that represents zero error and represents the highest error for each protocol/column.

Model	Sine Wave (Pr7)	AP (Pr6)	Steady Act. (Pr3)	Deact. (Pr5)	Inact. (Pr4)
New model for Cell #6	0.0113	0.0216	0.0264	0.0504	0.0170
Wang *et al.*[6]	0.0263	0.0273	0.0370	0.0299	0.0240
Di Veroli *et al.*[30]	0.0251	0.0375	0.0379	0.0492	0.0204
Mazhari *et al.*[15]	0.0319	0.0369	0.0324	0.0606	0.0292
ten Tusscher *et al.*[23]	0.0409	0.0451	0.0455	0.0603	0.0384
Zeng *et al.*[3]	0.0488	0.0644	0.0472	0.0688	0.0342

Table D8: Table quantifying mean square difference (units nA) between experimental current traces and simulation predictions for the validation protocols shown in Figures 4 and 5 for Cell #7. Here the color scale is set so that ■ represents zero error and ■ represents the highest error for each protocol/column.

Model	Sine Wave (Pr7)	AP (Pr6)	Steady Act. (Pr3)	Deact. (Pr5)	Inact. (Pr4)
New model for Cell #7	0.0495	0.0777	0.1446	0.1824	0.0655
Wang *et al.*[6]	0.1175	0.1394	0.1743	0.1392	0.0923
Di Veroli *et al.*[30]	0.1142	0.1541	0.2052	0.2382	0.0960
Mazhari *et al.*[15]	0.1485	0.1628	0.1410	0.2669	0.1303
ten Tusscher *et al.*[23]	0.1900	0.2102	0.2237	0.2726	0.1700
Zeng *et al.*[3]	0.2121	0.2567	0.2567	0.3177	0.1624

Table D9: Table quantifying mean square difference (units nA) between experimental current traces and simulation predictions for the validation protocols shown in Figures 4 and 5 for Cell #8. Here the color scale is set so that ■ represents zero error and ■ represents the highest error for each protocol/column.

Model	Sine Wave (Pr7)	AP (Pr6)	Steady Act. (Pr3)	Deact. (Pr5)	Inact. (Pr4)
New model for Cell #8	0.0294	0.0482	0.0551	0.0927	0.0510
Wang *et al.*[6]	0.0605	0.0625	0.1112	0.1258	0.0626
Di Veroli *et al.*[30]	0.0542	0.0753	0.0858	0.1415	0.0641
Mazhari *et al.*[15]	0.0700	0.0759	0.0893	0.1717	0.0831
ten Tusscher *et al.*[23]	0.0864	0.0940	0.1279	0.1810	0.1013
Zeng *et al.*[3]	0.0990	0.1168	0.1324	0.1909	0.0961

Table D10: Table quantifying mean square difference (units nA) between experimental current traces and simulation predictions for the validation protocols shown in Figures 4 and 5 for Cell #9. Here the color scale is set so that ■ represents zero error and ■ represents the highest error for each protocol/column.

Model	Sine Wave (Pr7)	AP (Pr6)	Steady Act. (Pr3)	Deact. (Pr5)	Inact. (Pr4)
New model for Cell #9	0.0183	0.0314	0.0361	0.0506	0.0294
Wang *et al.*[6]	0.0300	0.0351	0.0558	0.0483	0.0339
Di Veroli *et al.*[30]	0.0248	0.0307	0.0374	0.0531	0.0277
Mazhari *et al.*[15]	0.0262	0.0329	0.0407	0.0632	0.0315
ten Tusscher *et al.*[23]	0.0358	0.0421	0.0612	0.0673	0.0408
Zeng *et al.*[3]	0.0429	0.0470	0.0602	0.0709	0.0364

E Additional Current-Voltage Relationship Predictions

Here we show the remainder of the predictions of the current-voltage relationships for the validation data of cell 5 that were not included in the main text (the results of Pr1 and Pr2, and extra IV curves for Pr4). Figure E8 shows the summary curves for Pr1 (voltage clamp shown in Figure B3) and Pr2 (voltage clamp shown in Figure B4).

Traditionally these peak current curves would be plotted by normalizing to the peak current recorded in each activation kinetics protocol. However, as we have used a shorter version of the activation kinetics protocol, we do not expect that the channel would be fully open at the longest duration test step in Pr1 and Pr2. We have therefore instead normalized the curves using the peak current during the initial deactivation step in the sine wave protocol (around 1.6 seconds) where we expect the channel to be maximally open.

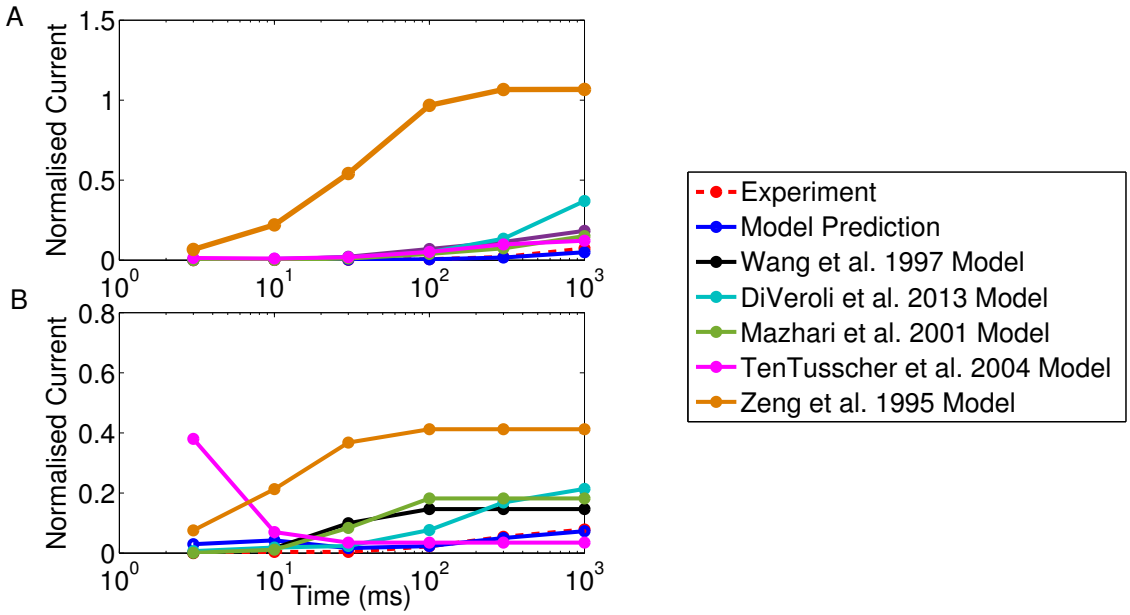

Figure E8: Predictions of peak current-voltage relationship derived from experiment and model predictions in response to; A) Activation Kinetics Pr1, B) Activation Kinetics Pr2, with comparison of our model prediction with predictions from existing literature models. Currents have been normalized to the peak current in the initial deactivation step in the sine wave protocol (around 1.6 seconds) as we do not expect the channel to be fully open at the longest T_{step} in these activation kinetics protocols.

In Figures E9 and E10 we plot additional IV curves summarising the experimental, New Model and literature model responses to the inactivation protocol Pr4.

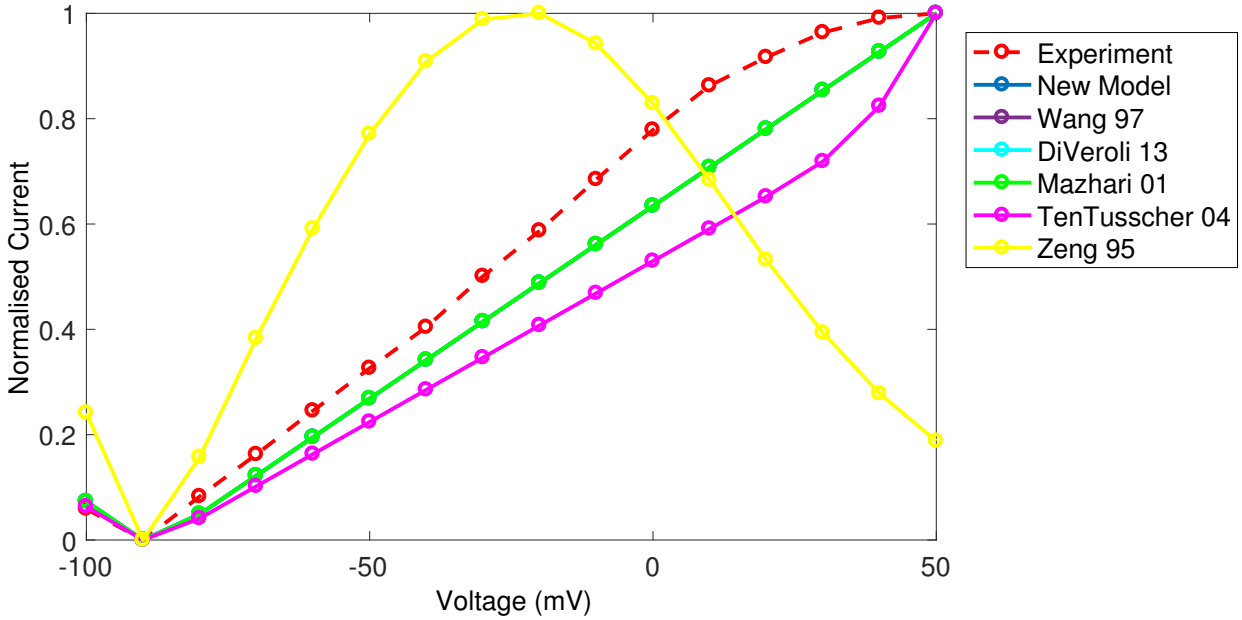

Figure E9: Inactivation peak current IV curve, summarizing currents in response to Pr4. The New Model, Wang, DiVeroli and Mazhari model IV curves are all indistinguishable here and lie on top of one another under the green line.

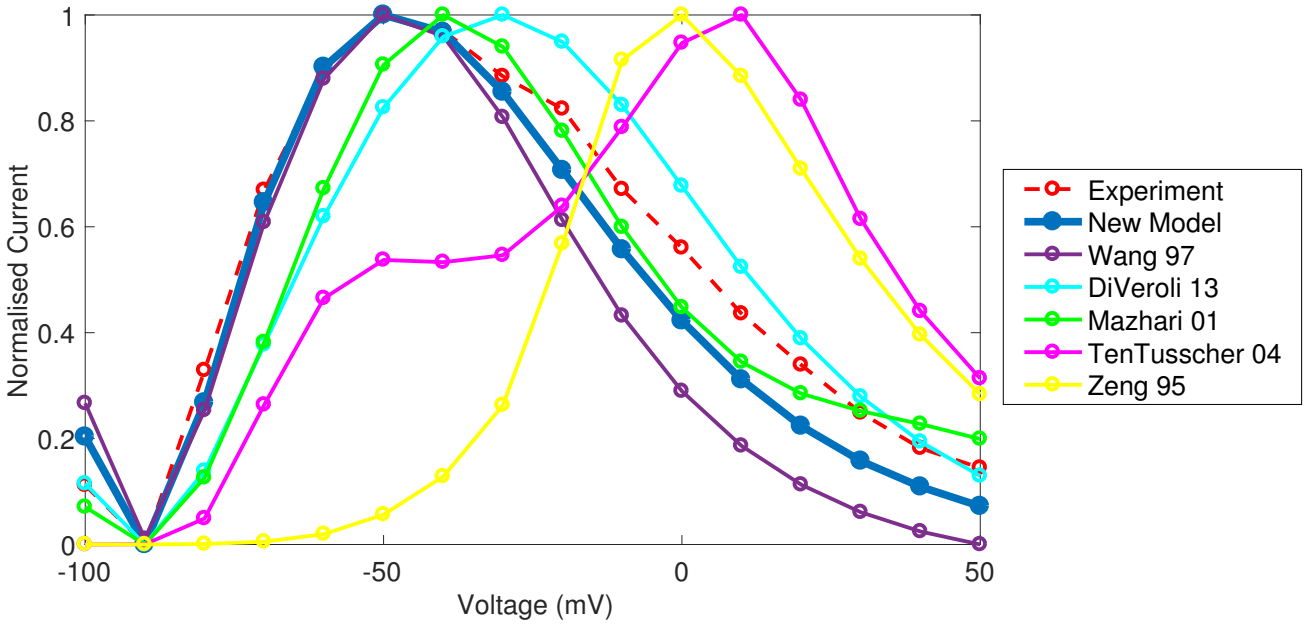

Figure E10: Inactivation steady-state current IV curve, summarizing currents in response to Pr4.

F Comparing Cell-Specific with Average Model

In addition to creating cell specific models as described so far we also created an averaged model by first normalizing each experimental trace to one reference trace (so that each trace was given equal weight in the averaging regardless of the conductance of the channel) and then summing and averaging the current value at each time point along the protocol.

The parameter values obtained when calibrating each cell-specific and averaged model are shown in Table F11. These values correspond to the parameter sets with maximum posterior density identified in the MCMC chain. The full posterior density distributions for each parameter for each of the 9 cells are shown in Figure F11.

Table F11: Table of parameter values at the maximum posterior density for each cell-specific model, and the model fitted to averaged data (N.B. not the average of the cell-specific parameters). Here the model parameter numberings correspond to those detailed in Figure 3B, and G_{Kr} represents the conductance value fitted for each model. *Note that the conductance fitted for the 'Averaged' model reflects mainly the conductance for the reference experimental trace (used for scaling all other traces before averaging), and should not be considered the 'average' conductance, hence its omission from Figure 6A.

	P_1	P_2	P_3	P_4	P_5	P_6	P_7	P_8	G_{Kr}
Cell #1	1.9800×10^{-4}	0.0593	7.1688×10^{-5}	0.0493	0.1048	0.0139	0.0038	0.0360	0.1351
Cell #2	3.2387×10^{-4}	0.0653	7.8195×10^{-5}	0.0497	0.0805	0.0025	0.0049	0.0324	0.0902
Cell #3	4.7771×10^{-4}	0.0661	5.1611×10^{-5}	0.0523	0.1375	0.0094	0.0039	0.0375	0.1011
Cell #4	6.7414×10^{-4}	0.0577	5.8027×10^{-5}	0.0517	0.0893	0.0057	0.0059	0.0324	0.0741
Cell #5	2.2603×10^{-4}	0.0699	3.4481×10^{-5}	0.0546	0.0873	0.0089	0.0052	0.0316	0.1524
Cell #6	6.1840×10^{-4}	0.0658	1.2754×10^{-4}	0.0379	0.0810	0.0165	0.0092	0.0253	0.0218
Cell #7	5.4045×10^{-4}	0.0484	6.5855×10^{-5}	0.0457	0.0627	0.0087	0.0054	0.0318	0.1553
Cell #8	3.1336×10^{-4}	0.0481	5.0647×10^{-5}	0.0491	0.0723	0.0063	0.0060	0.0328	0.0984
Cell #9	5.6194×10^{-4}	0.0433	1.2400×10^{-4}	0.0444	0.0659	0.0028	0.0036	0.0343	0.0514
Averaged	4.0000×10^{-4}	0.0579	6.5092×10^{-5}	0.0487	0.0807	0.0068	0.0052	0.0334	0.0673*

To quantitatively compare the average model predictions and the cell-specific model predictions shown in Figure 6B of the main text we calculated the mean square difference at each point between the average model and the cell-specific models for each cell when predicting the full current trace in response to the steady-state activation protocol. We also repeated this for the deactivation and inactivation protocols and the action potential protocol shown in Figures 4 and 5. The differences for each cell are shown in Table F12 with a comparison between the experimental result and the average model predictions with the cell-specific predictions.

We note that we have ordered the cells in this table (as in Figure 6) according to the percentage change in leak resistance between performing the vehicle and dofetilide repeats of the sine wave voltage protocol used to construct the model. This ordering acts as an estimated ranking for the quality of each recording. The benefit of a cell-specific approach occurs when using the highest quality data for both model construction and validation. We should note that even though in cells #4 and #6 the average model provides the better prediction of the steady-state activation peak current-voltage relationship than the cell-specific model, the cell-specific models are still providing very good predictions in these cases, it is just that the experimental behavior is more like the average model behavior for these cells. We also note that for eight out of the nine cells, the cell-specific model provides a better prediction of the current response to the action potential protocol than the average model, however, in the case where the cell-specific model is worse the difference is only a small amount.

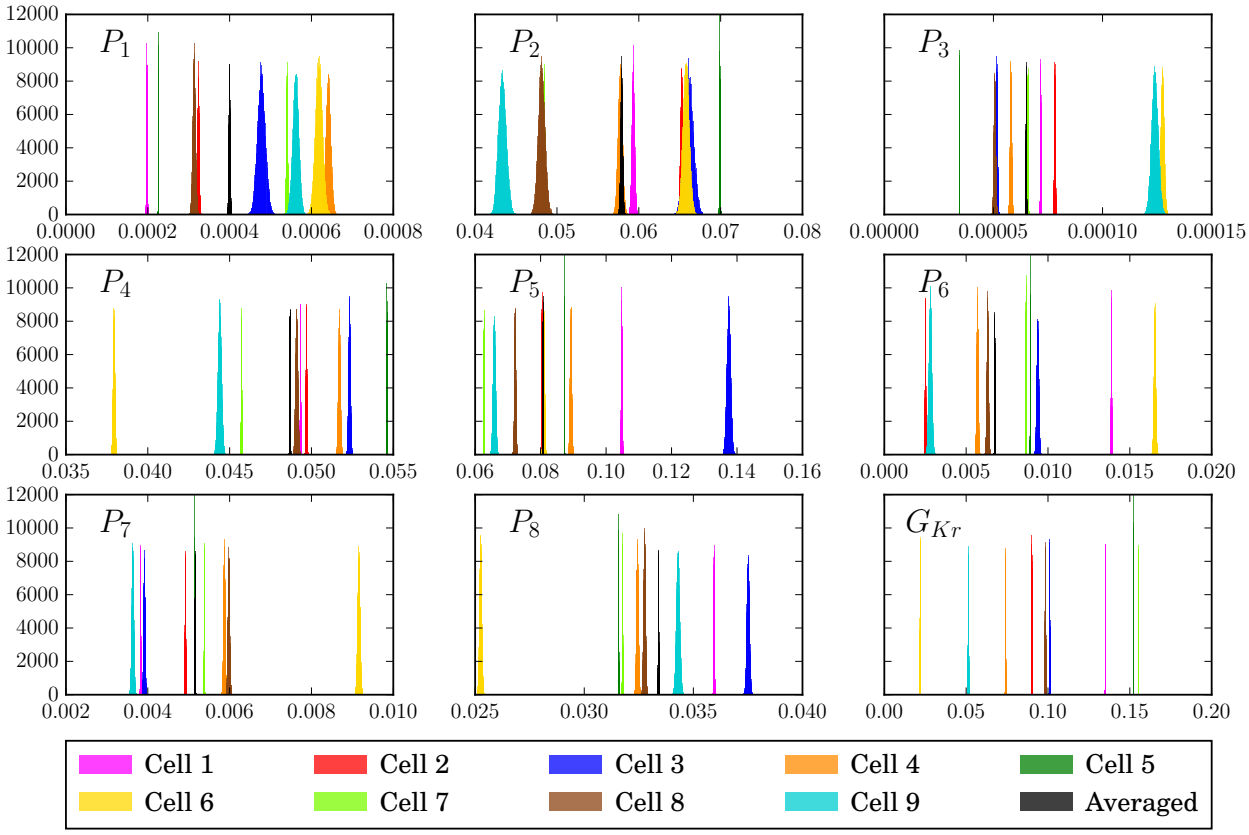

Figure F11: Distributions for each parameter for each of the 9 cell-specific models and the averaged data model. To aid comparison these are all histograms with 100 bars (plotting probability distributions here leads to very different maxima, obscuring the spread information), and so the y-axis is in arbitrary units related to the number of samples. We see that the parameter values tend to be given distinct distributions and so we would consider most of them to be 'significantly different', indicating that the variation we see in Figure 6 is due to cell-cell variability in the recordings rather than noise or unidentifiability in our parameter estimates.

We use a measure of

$$\text{error} = \frac{1}{T}\sum_{t=1}^{T}\Big((\text{simulated current at time step } t - \text{experimental current at time step } t)^2\Big)^{\frac{1}{2}}, \tag{F.10}$$

to evaluate the error in model predictions for individual cells (using the whole current traces, apart from removing regions in the sine wave protocol with capacitive spikes as explained in Methods B2.1).

Table F12: Table showing the error measure defined by equation F.10 between cell-specific or average models and the experimental current recording for fit (sine wave Pr7) and predictions with validation protocols (all other columns). Cells are ordered in ascending order according to the percentage change in leak resistance R_{leak}. Here the color scale is set so that within each pair of columns represents lowest error and represents the highest error for each protocol/pair of columns. Note that the cells with larger currents will show larger errors, but the left column cell-specific predictions tend to perform better than the average model, particularly for cells where the average model gives a relatively large error.

Cell	ΔR_{leak}	Sine Wave (Pr 7)		APs (Pr 6)		Steady Act. (Pr 3)		Deact. (Pr 4)		Inact. (Pr 5)	
#	(%)	Specific	Average	Spec.	Aver.	Spec.	Aver.	Spec.	Aver.	Spec.	Aver.
1	0.0	0.0151	0.0367	0.0283	0.0567	0.0332	0.0770	0.0925	0.1138	0.0312	0.0372
2	7.7	0.0164	0.0271	0.0295	0.0343	0.0270	0.0334	0.0656	0.0619	0.0219	0.0237
3	12.5	0.0253	0.0406	0.0415	0.0681	0.0658	0.1111	0.0785	0.0869	0.0537	0.0731
4	16.7	0.0258	0.0318	0.0359	0.0411	0.0701	0.0580	0.0878	0.0846	0.0522	0.0563
5	20.0	0.0203	0.0228	0.0453	0.0535	0.0437	0.0591	0.1317	0.1608	0.0700	0.0668
6	28.6	0.0113	0.0205	0.0216	0.0250	0.0264	0.0206	0.0504	0.0435	0.0170	0.0183
7	32.5	0.0495	0.0631	0.0777	0.0885	0.1446	0.1198	0.1824	0.2016	0.0655	0.0740
8	42.9	0.0294	0.0352	0.0482	0.0507	0.0551	0.0603	0.0927	0.1265	0.0510	0.0526
9	58.3	0.0183	0.0195	0.0314	0.0306	0.0361	0.0321	0.0506	0.0462	0.0294	0.0294

For predictions of the action potential protocol currents, Table F12 demonstrates that the cell-specific modeling approach yields predictions that are very close to or better than the average model. Additionally, for the predictions of the steady-state activation protocol the cell-specific approach generally yields very good and more accurate (for 4/5) predictions of validation data when the highest quality data is used (cells #1–5). This benefit is absent when lower quality experimental data is used where the average model provides very similar, but slightly better, predictions (cells #6–9).

We also compare cell-specific and average predictions for each of the 9 cells for the deactivation, recovery from inactivation and instantaneous inactivation time constants as were shown for one cell in Figure 4. We show this comparison for each cell in Figure F12 and F13 for 8/9 cells and in Figure F14 for all cells. Cell #6 was omitted in the first two plots because this cell had a particularly low current and it was difficult to accurately fit exponential curves to the experimental data for this cell. We also note that we have not plotted the time constant values for $-90\,\text{mV}$ in Figures F12 & F13 for the same reason; we could not confidently fit an exponential decay curve to determine an accurate time constant value for this voltage step.

We see in Figures F12–F14 that the same observations that were made for the results shown in Figure 6 generally hold: for lower cell numbers #1–5, we see enhanced predictions of the experimental time constants from the cell-specific model rather than the averaged model. i.e predictions are better in the cells with lower percentage changes in leak current resistance, which correspond

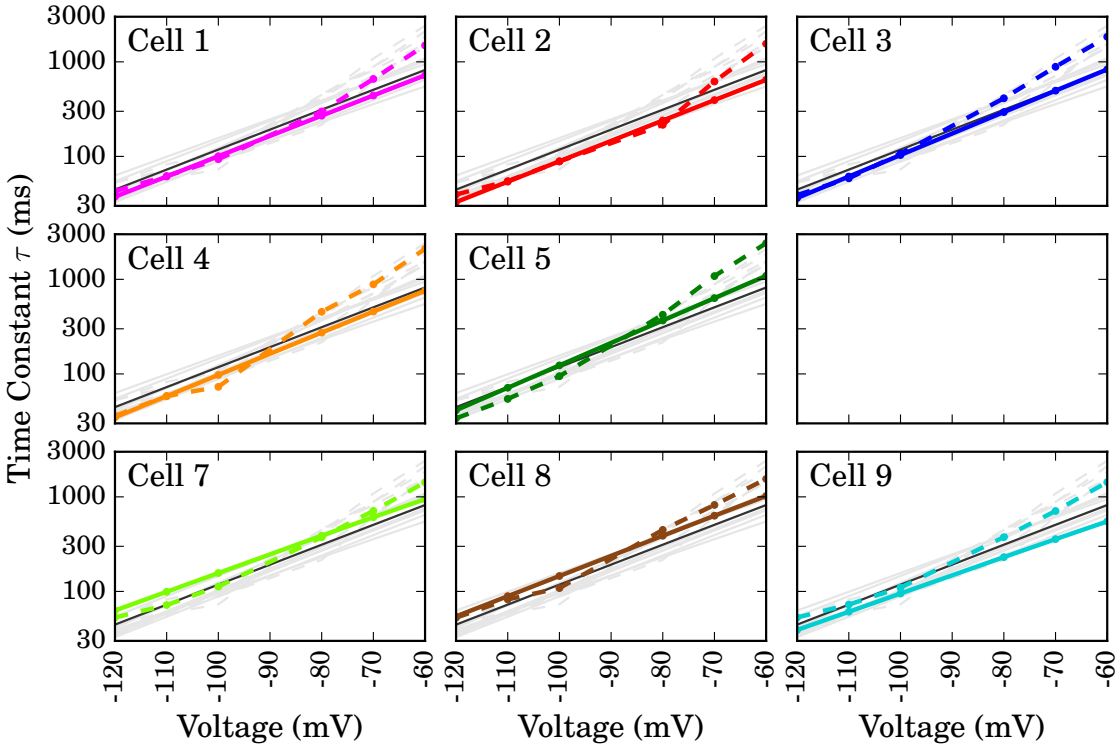

Figure F12: Cell-specific model predictions of time constant/voltage relationships for deactivation (Pr5). Each plot represents a different cell, with cell-specific model prediction depicted by the bold line, and the dashed line showing the cell's experimental data. Black lines on each plot represents the average model prediction. Cells are ordered as in Table F12.

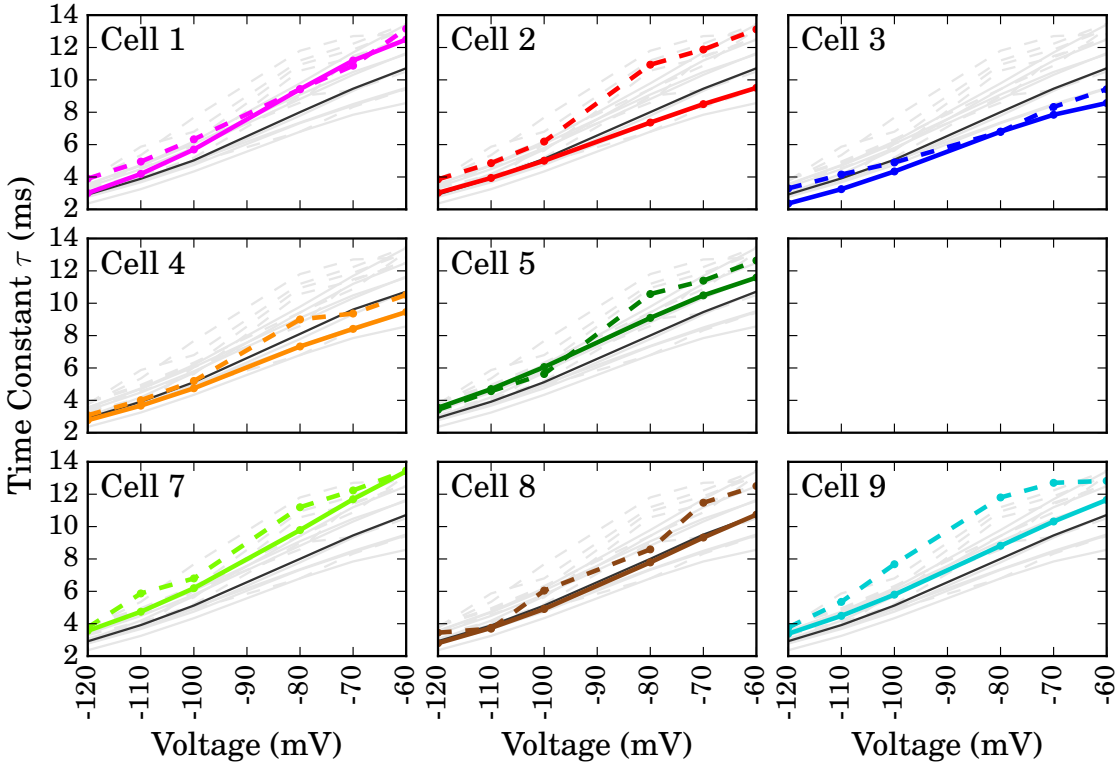

Figure F13: Cell-specific model predictions of time constant/voltage relationships for recovery from inactivation in Pr5. Each plot represents a different cell, with cell-specific model prediction depicted by the bold line, and the dashed line showing the cell's experimental data. Black lines on each plot represents the average model prediction. Cells are ordered as in Table F12.

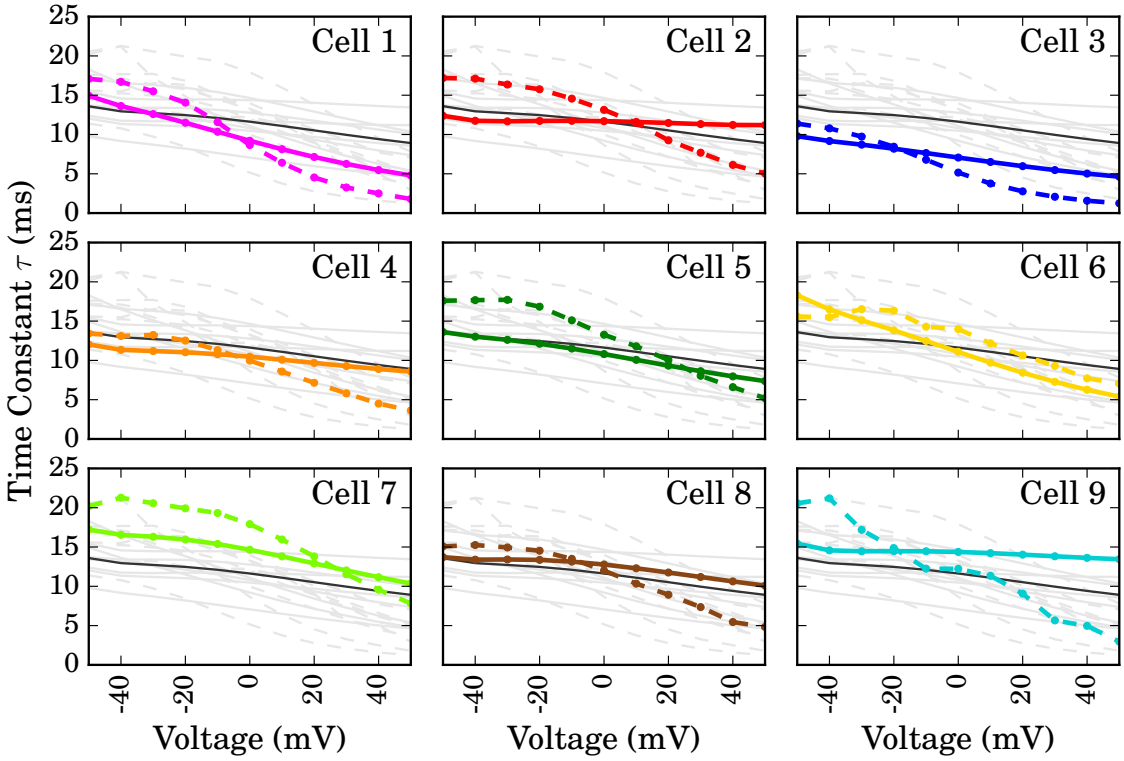

Figure F14: Cell-specific model predictions of time constant/voltage relationships for instantaneous inactivation (Pr4). Each plot represents a different cell, with cell-specific model prediction depicted by the bold line, and the dashed line showing the cell's experimental data. Black lines on each plot represents the average model prediction. Cells are ordered as in Table F12.

to better quality data.

G Wider applicability: synthetic data study for an I_{Ks} model

In order to demonstrate the wider applicability of our approach we also show its suitability for parameterising a model of a different ion current — the slowly activating delayed rectifier potassium channel (I_{Ks}). We tested the approach using a synthetic data study similar to that described in Section C2 for the model in the main text. The I_{Ks} model we used was taken from the ten Tusscher *et al.*[23] cardiac action potential model which (including a conductance parameter) has 8 parameters within the I_{Ks} model. The model, which we have rewritten to make all parameters *a priori* identifiable, takes the form shown in Equations (G.11)–(G.16):

$$I_{Ks} = G_{Ks} X_s^2 (V - E_{Ks}), \tag{G.11}$$

$$Xs_\infty = \frac{1}{1 + P_1 \exp(-P_2 V)}, \tag{G.12}$$

$$\alpha_{Xs} = \frac{1}{1 + P_6 \exp(P_7 V)}, \tag{G.13}$$

$$\beta_{Xs} = \frac{1}{P_5 \sqrt{1 + P_3 \exp(-P_4 V)}}, \tag{G.14}$$

$$\tau_{Xs} = \alpha_{Xs} \beta_{Xs}, \tag{G.15}$$

$$\frac{\mathrm{d}X_s}{\mathrm{d}t} = \frac{Xs_\infty - X_s}{\tau_{Xs}}. \tag{G.16}$$

In Table G13 we compare the parameters we used to generate the synthetic data and the parameters we identified as producing the best fit to these synthetic data (which included added noise). We see that the maximum likelihood parameters are very similar to those from which the synthetic data were produced, demonstrating the theoretical capability of this approach to parameterise a model of I_{Ks}. The practicality of this approach with real data is still to be explored.

Table G13: Table comparing parameter values used to simulate the synthetic data for the I_{Ks} model and the maximum likelihood fit to these data.

	P_1	P_2	P_3	P_4	P_5	P_6	P_7	G_{Kr}
Underlying Synthetic Data Value	0.6997	0.0714	0.1889	0.1667	0.0009	0.0498	0.05	0.1
Fitted Value	0.6967	0.0716	0.1964	0.1659	0.0009	0.0540	0.0486	0.0999

References

1. Kiehn, J., Lacerda, A. & Brown, A. Pathways of HERG inactivation. *American Journal of Physiology-Heart and Circulatory Physiology* **277,** H199–H210 (1999).
2. Piper, D., Varghese, A., Sanguinetti, M. & Tristani-Firouzi, M. Gating currents associated with intramembrane charge displacement in HERG potassium channels. *Proceedings of the National Academy of Sciences* **100,** 10534 (2003).
3. Zeng, J., Laurita, K. R., Rosenbaum, D. S. & Rudy, Y. Two components of the delayed rectifier K+ current in ventricular myocytes of the guinea pig type theoretical formulation and their role in repolarization. *Circulation Research* **77,** 140–152 (1995).
4. Lindblad, D., Murphey, C., Clark, J. & Giles, W. A model of the action potential and underlying membrane currents in a rabbit atrial cell. *American Journal of Physiology* **271,** H1666–H1696 (1996).
5. Liu, S., Rasmusson, R., Campbell, D., Wang, S. & Strauss, H. Activation and inactivation kinetics of an E-4031-sensitive current from single ferret atrial myocytes. *Biophysical Journal* **70,** 2704–2715 (1996).
6. Wang, S., Liu, S., Morales, M., Strauss, H. & Rasmusson, R. A quantitative analysis of the activation and inactivation kinetics of HERG expressed in Xenopus oocytes. *Journal of Physiology* **502,** 45–60 (1997).
7. Courtemanche, M., Ramirez, R. & Nattel, S. Ionic mechanisms underlying human atrial action potential properties: Insights from a mathematical model. *American Journal of Physiology-Heart and Circulatory Physiology* **275,** H301–H321 (1998).
8. Nygren, A., Fiset, C., Firek, L., Clark, J., Lindblad, D., Clark, R. & Giles, W. Mathematical model of an adult human atrial cell the role of K+ currents in repolarization. *Circulation Research* **82,** 63–81 (1998).
9. Priebe, L. & Beuckelmann, D. J. Simulation study of cellular electric properties in heart failure. *Circulation Research* **82,** 1206–1223 (1998).
10. Winslow, R. L., Rice, J., Jafri, S., Marban, E. & O'Rourke, B. Mechanisms of altered excitation-contraction coupling in canine tachycardia-induced heart failure, II Model studies. *Circulation Research* **84,** 571–586 (1999).
11. Ramirez, R. J., Nattel, S. & Courtemanche, M. Mathematical analysis of canine atrial action potentials: rate, regional factors, and electrical remodeling. *American Journal of Physiology-Heart and Circulatory Physiology* **279,** H1767–H1785 (2000).
12. Zhang, H., Holden, A., Kodama, I., Honjo, H., Lei, M., Varghese, T. & Boyett, M. Mathematical models of action potentials in the periphery and center of the rabbit sinoatrial node. *American Journal of Physiology-Heart and Circulatory Physiology* **279,** H397–H421 (2000).
13. Clancy, C. & Rudy, Y. Cellular consequences of HERG mutations in the long QT syndrome: Precursors to sudden cardiac death. *Cardiovascular Research* **50,** 301–313 (2001).
14. Lu, Y., Mahaut-Smith, M., Varghese, A., Huang, C., Kemp, P. & Vandenberg, J. Effects of premature stimulation on HERG K+ channels. *The Journal of Physiology* **537,** 843–851 (2001).
15. Mazhari, R., Greenstein, J., Winslow, R., Marbán, E. & Nuss, H. Molecular interactions between two Long-QT syndrome gene products, HERG and KCNE2, rationalized by in vitro and in silico analysis. *Circulation Research* **89,** 33–38 (2001).

16. Fox, J. J., McHarg, J. L. & Gilmour Jr, R. F. Ionic mechanism of electrical alternans. *American Journal of Physiology-Heart and Circulatory Physiology* **282,** H516–H530 (2002).

17. Kurata, Y., Hisatome, I., Imanishi, S. & Shibamoto, T. Dynamical description of sinoatrial node pacemaking: improved mathematical model for primary pacemaker cell. *American Journal of Physiology-Heart and Circulatory Physiology* **283,** H2074–H2101 (2002).

18. Oehmen, C., Giles, W. & Demir, S. Mathematical model of the rapidly activating delayed rectifier potassium current IKr in rabbit sinoatrial node. *Journal of Cardiovascular Electrophysiology* **13,** 1131–1140 (2002).

19. Matsuoka, S., Sarai, N., Kuratomi, S., Ono, K. & Noma, A. Role of individual ionic current systems in ventricular cells hypothesized by a model study. *The Japanese Journal of Physiology* **53,** 105–123 (2003).

20. Seemann, G., Sachse, F. B., WEIß, D. L. & DÖSSEL, O. Quantitative reconstruction of cardiac electromechanics in human myocardium. *Journal of Cardiovascular Electrophysiology* **14,** S219–S228 (2003).

21. Hund, T. J. & Rudy, Y. Rate dependence and regulation of action potential and calcium transient in a canine cardiac ventricular cell model. *Circulation* **110,** 3168–3174 (2004).

22. Shannon, T., Wang, F., Puglisi, J., Weber, C. & Bers, D. A mathematical treatment of integrated Ca dynamics within the ventricular myocyte. *Biophysical Journal* **87,** 3351–3371 (2004).

23. Ten Tusscher, K., Noble, D., Noble, P. & Panfilov, A. A model for human ventricular tissue. *American Journal of Physiology-Heart and Circulatory Physiology* **286,** H1573–H1589 (2004).

24. Fink, M., Noble, D., Virag, L., Varro, A. & Giles, W. R. Contributions of HERG K+ current to repolarization of the human ventricular action potential. *Progress in Biophysics and Molecular Biology* **96,** 357–376 (2008).

25. Aslanidi, O. V., Stewart, P., Boyett, M. R. & Zhang, H. Optimal velocity and safety of discontinuous conduction through the heterogeneous Purkinje-ventricular junction. *Biophysical Journal* **97,** 20–39 (2009).

26. Inada, S., Hancox, J., Zhang, H. & Boyett, M. One-dimensional mathematical model of the atrioventricular node including atrio-nodal, nodal, and nodal-his cells. *Biophysical Journal* **97,** 2117–2127 (2009).

27. Grandi, E., Pasqualini, F. S. & Bers, D. M. A novel computational model of the human ventricular action potential and Ca transient. *Journal of Molecular and Cellular Cardiology* **48,** 112–121 (2010).

28. O'Hara, T., Virág, L., Varró, A. & Rudy, Y. Simulation of the undiseased human cardiac ventricular action potential: model formulation and experimental validation. *PLoS Computational Biology* **7,** e1002061 (2011).

29. Severi, S., Fantini, M., Charawi, L. A. & DiFrancesco, D. An updated computational model of rabbit sinoatrial action potential to investigate the mechanisms of heart rate modulation. *The Journal of Physiology* **590,** 4483–4499 (2012).

30. Di Veroli, G., Davies, M., Zhang, H., Abi-Gerges, N. & Boyett, M. High-throughput screening of drug-binding dynamics to HERG improves early drug safety assessment. *American Journal of Physiology-Heart and Circulatory Physiology* **304,** H104–H117 (2013).

31. Lacroix, J. J., Labro, A. J. & Bezanilla, F. Properties of deactivation gating currents in Shaker channels. *Biophysical Journal* **100,** L28–L30 (2011).

32. Walch, O. J. & Eisenberg, M. C. Parameter identifiability and identifiable combinations in generalized Hodgkin–Huxley models. *Neurocomputing* **199,** 137–143 (2016).

33. Vandenberg, J., Perry, M., Perrin, M., Mann, S., Ke, Y. & Hill, A. hERG K+ channels: Structure, function, and clinical significance. *Physiological Reviews* **92,** 1393–1478 (2012).

34. Haario, H., Saksman, E. & Tamminen, J. An Adaptive Metropolis Algorithm. *Bernoulli,* 223–242 (2001).

35. Gilks, W. R., Richardson, S. & Spiegelhalter, D. J. *Markov Chain Monte Carlo in Practice* (London: Chapman and Hall, 1996).